

ADAPTIVE FINITE ELEMENTS FOR OBSTACLE PROBLEMS

TOM GUSTAFSSON[†]

ABSTRACT. We summarise three applications of the obstacle problem to membrane contact, elastoplastic torsion and cavitation modelling, and show how the resulting models can be solved using mixed finite elements. It is challenging to construct fixed computational meshes for any inequality-constrained problem because the coincidence set has an unknown shape. Consequently, we demonstrate how h -adaptivity can be used to resolve the unknown coincidence set. We demonstrate some practical challenges that must be overcome in the application of the adaptive method.

This preprint corresponds to the Chapter 5 of volume 58 in AAMS, Advances in Applied Mechanics.

[†]*Department of Mechanical Engineering, Aalto University*

1. INTRODUCTION

Let $\Omega \subset \mathbb{R}^2$ be a computational domain. The classical obstacle problem can be written as follows: find $u : \Omega \rightarrow \mathbb{R}$ such that

$$(1) \quad -\Delta u \geq f, \quad u \geq g, \quad (\Delta u + f)(u - g) = 0, \quad u|_{\partial\Omega} = 0,$$

where f and g are given. The third condition implies that in some unknown coincidence set $\Omega_C \subset \Omega$ it holds $u = g$ while in $\Omega \setminus \Omega_C$ it holds $-\Delta u = f$. Because Ω_C is unknown a priori, it is challenging to construct computational meshes without relying to mesh adaptivity. In particular, more elements are usually required near the interface between the coincidence set and its complement, and the location and the shape of the interface are solution-dependent.

In this chapter, we review the following classical applications of the obstacle problem: membrane contact problem [1], elastoplastic torsion problem [2], and cavitation modelling of hydrodynamic bearings [3]. We formulate the corresponding Lagrange multiplier formulation and demonstrate numerically how a conforming h -adaptive and bubble-enriched $P_2 - P_0$ mixed finite element method analysed in [1] performs in each of the three applications. Other examples of obstacle-type problems are found, e.g., in flows through porous media [4], and in financial mathematics [5].

Closely related but more general problems where similar conclusions hold and, hence, analogous conforming finite element techniques work equally well are the frictionless contact problems of plates [6] and elastic bodies [7]. However, we note that while conforming methods have been introduced also for frictional contact problems [8] and some problems in plasticity [9], more general problems with constraints for the length of a vectorial variable seem to be better approximated using nonconforming methods; see also the recent monograph on the finite element approximation of contact and friction problems [10].

The method described in this chapter is just one among many approaches for solving obstacle problems, and has been chosen based on its low polynomial order, simplicity and well understood theoretical properties such as stability, a priori and a posteriori error estimates; cf., e.g., [11, 12, 13, 14, 15, 1]. Other approaches for solving the obstacle problem include (but are not limited to) the penalty method [16], Nitsche's method [2], augmented Lagrangian method [17], and the stabilised method [1].

In the following, we occasionally refer to the constrained minimisation form of the obstacle problem (1), i.e.

$$(2) \quad \inf_{\substack{u \in H_0^1(\Omega), \\ u \geq g}} \frac{1}{2}(\nabla u, \nabla u) - (f, u)$$

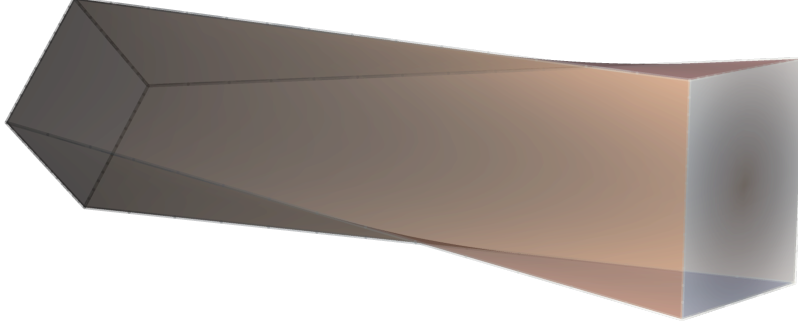


FIGURE 1. A visualisation of the kinematics of the torsion problem, $\vec{u}(x, y, z) = (-\theta yz, \theta xz, 0)$, when applied to a square shaft. The coordinate z is along the length of the shaft and θ refers to the magnitude of the rotation. The colouring is based on the magnitude of the displacement field with darker hue corresponding to smaller displacement magnitude.

where (\cdot, \cdot) denotes the L^2 inner product and $H_0^1(\Omega)$ refers to the set of functions with finite energy,

$$(\nabla u, \nabla u) < \infty,$$

and vanishing boundary values, $u|_{\partial\Omega} = 0$. For more details on the related function spaces we refer to [18].

2. APPLICATIONS

We now review three applications where a problem of the form (1) and (2) will arise.

2.1. Deformation and contact of a membrane. Consider a thin membrane, e.g. $D = \Omega \times [0, t]$ where $\Omega \subset \mathbb{R}^2$ describes the shape of the membrane on xy -plane and the thickness $t > 0$ is very small. We wish to describe the displacement $\vec{u} : D \rightarrow \mathbb{R}^3$ of the membrane under a body loading $\vec{f} = (0, 0, f)$. Under the kinematic assumption $\vec{u} = (0, 0, u(x, y))$, infinitesimal strain $\varepsilon = \frac{1}{2}(\nabla \vec{u} + \nabla \vec{u}^T)$, and the constitutive equation

$$\sigma = 2G\varepsilon + \left(K - \frac{2G}{3}\right) \text{tr} \varepsilon I,$$

the stress tensor evaluates to

$$\sigma = \begin{pmatrix} 0 & 0 & Gu_x \\ 0 & 0 & Gu_y \\ Gu_x & Gu_y & 0 \end{pmatrix}$$

where $G > 0$ is the shear modulus and $K > 0$ is the bulk modulus of the material. Consequently, the governing equation is simplified:

$$-\text{div} \sigma = \vec{f} \text{ in } D \quad \Rightarrow \quad -G\Delta u = f \text{ in } \Omega.$$

This is an obstacle problem if the membrane is constrained to lie above a rigid body, $u \geq g$, whose boundary is at the distance g below the membrane. The corresponding constrained minimisation problem reads

$$\inf_{\substack{u \in H_0^1(\Omega), \\ u \geq g}} \frac{1}{2}(G\nabla u, \nabla u) - (f, u)$$

where the membrane fixed on the boundary. The coincidence set Ω_C is interpreted as the zone where the rigid body and the membrane are in contact. Furthermore, the strong formulation reads: find $u : \Omega \rightarrow \mathbb{R}$ such that

$$(3) \quad -\nabla \cdot G\nabla u \geq f, \quad u \geq g, \quad (-\nabla \cdot G\nabla u + f)(u - g) = 0, \quad u|_{\partial\Omega} = 0,$$

2.2. Elastoplastic torsion problem. Consider a uniform shaft $D = \Omega \times [0, L]$ where $\Omega \subset \mathbb{R}^2$ is the shape of the cross section and L is the length of the shaft. The kinematic assumption $\vec{u}(x, y, z) = (-\theta yz, \theta xz, 0)$, $0 < z < L$, $\theta > 0$, describes a (small) rotation on xy -plane whose magnitude varies linearly along the shaft while the twist per unit length θ is a given constant and has units radians/meter, see Figure 1. A similar derivation of the torsion problem without plasticity can be found in Feng–Shi [19].

As above, evaluating the infinitesimal strain and the stress tensor reveals the nonzero stress components

$$\sigma_{zx} = -G\theta y, \quad \sigma_{zy} = G\theta x.$$

Differentiating with respect to y and x , respectively, and summing the two formulae leads to

$$-\partial_y \sigma_{zx} + \partial_x \sigma_{zy} = 2G\theta.$$

By introducing the stress function ϕ so that

$$\partial_y \phi = \sigma_{zx} \quad \text{and} \quad -\partial_x \phi = \sigma_{zy},$$

the above equation becomes

$$-\Delta \phi = 2G\theta \text{ in } \Omega.$$

The shaft is assumed to be traction free on the boundary of the cross section. This is written in terms of stress as

$$\sigma_{zx} n_x + \sigma_{zy} n_y = 0$$

and, consequently, in terms of the stress function as

$$\partial_y \phi n_x - \partial_x \phi n_y = 0,$$

i.e. the tangential derivative of ϕ is zero along the boundary. This implies that ϕ is constant over the boundary but since we are only interested in the derivatives of ϕ and not its value, we can simply set $\phi|_{\partial\Omega} = 0$.

In reality there is an upper bound for the stress. For example, the von Mises yield criterion becomes

$$\sqrt{3(\sigma_{zx}^2 + \sigma_{zy}^2)} \leq \tau,$$

or, in terms of the stress function,

$$(4) \quad |\nabla \phi| \leq \frac{\tau}{\sqrt{3}},$$

where $\tau > 0$ is a given yield stress.

While (4) is an upper bound for the gradient of the stress function, Brezis–Sibony [20] show the nontrivial result that the minimisation problem

$$\inf_{\substack{\phi \in H_0^1(\Omega), \\ |\nabla \phi| \leq \frac{\tau}{\sqrt{3}}}} \frac{1}{2} (\nabla \phi, \nabla \phi) - (2G\theta, \phi)$$

can be reformulated as

$$\inf_{\substack{\phi \in H_0^1(\Omega), \\ \phi \leq \frac{\tau \delta}{\sqrt{3}}}} \frac{1}{2} (\nabla \phi, \nabla \phi) - (2G\theta, \phi)$$

where $\delta : \Omega \rightarrow \mathbb{R}$ is the distance to the boundary, i.e.

$$\delta(\vec{x}) = \inf_{\vec{y} \in \partial\Omega} |\vec{x} - \vec{y}|.$$

The coincidence set Ω_C is interpreted as the zone where plastic deformation will occur. The bound for ϕ is from above, but if we define $\psi = -\phi$, we may instead consider the following strong formulation: find $\psi : \Omega \rightarrow \mathbb{R}$ such that

$$(5) \quad -\Delta \psi \geq -2G\theta, \quad \psi \geq -\frac{\tau \delta}{\sqrt{3}}, \quad (\Delta \psi - 2G\theta) \left(\psi + \frac{\tau \delta}{\sqrt{3}} \right) = 0, \quad \psi|_{\partial\Omega} = 0.$$

2.3. Hydrodynamic lubrication with cavitation. Hydrodynamic bearings are often modelled using the Reynolds equation [21]. The Reynolds equation for the pressure p within a thin film of lubricant, situated between two approximately parallel surfaces, one moving at the velocity V and at the distance d while the other is fixed, reads

$$(6) \quad \nabla \cdot \frac{d^3}{\mu} \nabla p = 6V \frac{\partial d}{\partial x},$$

where μ is the dynamic viscosity of the lubricant. The derivation is presented in several references; cf. [21, 22, 23]. The assumptions of the model are:

- (1) The lubricant is incompressible and Newtonian.
- (2) The fluid film thickness d is small with respect to the characteristic length along other dimensions.
- (3) The curvature of the surfaces is negligible.
- (4) The flow is slow enough so that the inertia can be ignored.

The geometry of an ideal hydrodynamic bearing, i.e. the gap between the housing and the shaft where the lubricant is situated, is defined by the equation

$$(7) \quad d(\theta) = c_1(1 + e \cos(\theta)), \quad -\pi < \theta < \pi,$$

where c_1 is the bearing clearance, e is the eccentricity, $0 \leq e < 1$. We wish to solve (6) on a rectangular domain $\Omega = (-R\pi, R\pi) \times (0, L)$ with periodic boundary conditions in $x = R\theta$, where R is the radius of the bearing and L is the width of the bearing, see Figure 2.

Solving Reynolds equation (6) with the bearing geometry (7), boundary conditions $p(-R\pi, y) = p(R\pi, y)$, $p(x, 0) = p(x, L) = p_{\text{env}}$ and $e \gg 0$ will result in subatmospheric pressures on the divergent region of the bearing. The zone of low pressure is subject to *cavitation* which means that any gas dissolved within the lubricant may expand or the lubricant may vaporise and cause lubrication film rupture [24]. While the physical mechanisms behind cavitation are complex, one goal of theoretical cavitation modelling is to incorporate film rupture into the Reynolds equation in an approximate manner.

The simplest cavitation model, known as the *Swift–Stieber cavitation inception condition* [24, p. 324], states that

$$(8) \quad \frac{\partial p}{\partial x} = \frac{\partial p}{\partial y} = 0, \quad p = p_{\text{cav}},$$

where p_{cav} is a constant known as the *cavitation pressure*. While there exist several advanced cavitation models that are physically more justified [24, p. 324–325], this simple model has the benefit that it becomes an obstacle problem which is well-posed and for which exist several well understood numerical methods: find $p : \Omega \rightarrow \mathbb{R}$ such that

$$-\nabla \cdot \frac{d^3}{\mu} \nabla p \geq -6V \frac{\partial d}{\partial x}, \quad p \geq p_{\text{cav}}, \quad \left(\nabla \cdot \frac{d^3}{\mu} \nabla p - 6V \frac{\partial d}{\partial x} \right) (p - p_{\text{cav}}) = 0,$$

and

$$p(-R\pi, y) = p(R\pi, y), \quad p(x, 0) = p(x, L) = p_{\text{env}}.$$

The coincidence set Ω_C is the set of points where cavitation is likely to occur.

3. VARIATIONAL FORMULATION

Due to the unknown coincidence set Ω_C , inequality-constrained problems are nonlinear and, hence, linearised to be solved iteratively. Some traditional approaches to inequality-constrained problems first discretise and then reintroduce inequality constraints at the discrete level either by penalising or through nodewise Lagrange multipliers. These techniques may be suitable for a fixed mesh and a constant obstacle but mesh adaptivity will require imposing the inequality constraints at a continuous level.

We will apply the method of Lagrange multipliers due to the following reasons: (1) this will lead to an error estimate also for the Lagrange multiplier which may have a physical interpretation such as the contact force, (2) the Lagrange multiplier, or an analogous quantity, is required in all finite element error indicators we are aware of, (3) we subjectively feel that this approach has the closest connection between the theory and the implementation of the method, (4) the implementation does not require a reassembly of the Jacobian if implemented as a primal-dual active set method as demonstrated in Section 3.2. Another feasible approach,

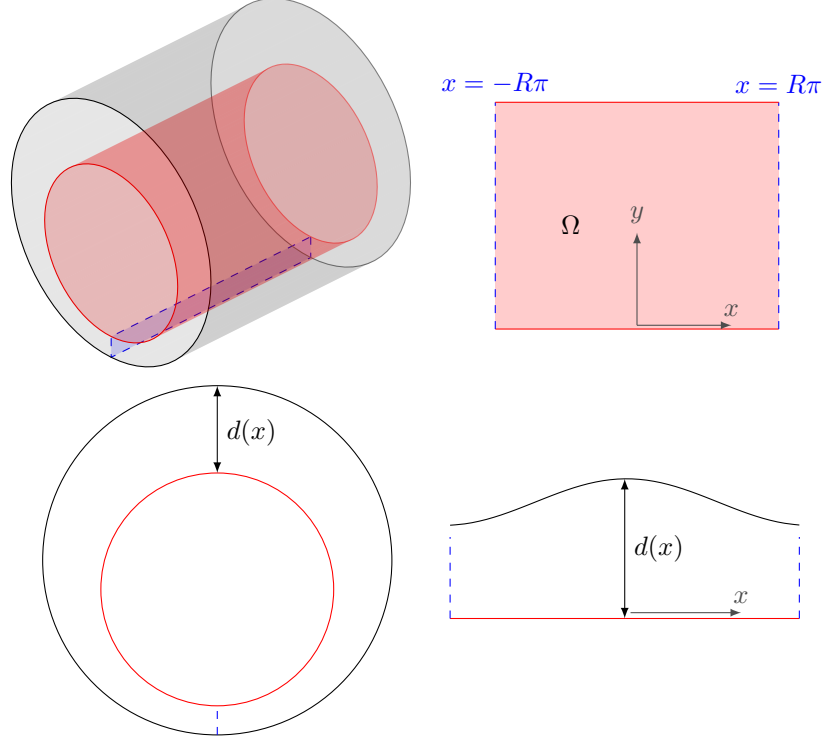


FIGURE 2. A schematic of a hydrodynamic bearing (top left), and its unraveled planar representation in a computational domain $\Omega = (-R\pi, R\pi) \times (0, L)$ (top right). The red cylinder represents a shaft which is fitted inside the bearing represented by the gray cylinder. The space between the shaft and the bearing is filled by a thin layer of lubricant with thickness $d(x)$. The lubricant pressure is periodic over the dashed parts of the boundaries.

not discussed here, is the use of Nitsche's method [1, 2] with the added benefit that the resulting linear system can be made positive definite while the benefit of (4) is lost.

Hence, by defining a new variable $\lambda = -\Delta u - f$, we arrive at the alternative formulation: find $u : \Omega \rightarrow \mathbb{R}$ and $\lambda : \Omega \rightarrow \mathbb{R}$ such that

$$-\Delta u - \lambda = f, \quad \lambda \geq 0, \quad u \geq g, \quad \lambda(u - g) = 0, \quad u|_{\partial\Omega} = 0.$$

From energy minimisation point-of-view, the new variable λ can be interpreted as a Lagrange multiplier for imposing the constraint $u \geq g$ a.e. in Ω . In particular, the minimisation problem

$$\inf_{\substack{u \in V, \\ u \geq g}} \frac{1}{2}(\nabla u, \nabla u) - (f, u)$$

can be alternatively written as the saddle point problem

$$\inf_{u \in V} \sup_{\lambda \in \Lambda} \frac{1}{2}(\nabla u, \nabla u) - (f, u) - \langle \lambda, u - g \rangle$$

where we have used the notation $\langle \cdot, \cdot \rangle : V' \times V \rightarrow \mathbb{R}$ for the duality pairing between the space V and its topological dual space V' , and the correct function spaces using standard notation for the Sobolev spaces read

$$V = H_0^1(\Omega), \quad Q = H^{-1}(\Omega), \quad \Lambda = \{\mu \in Q : \langle \mu, v \rangle \geq 0 \forall v \in V, v \geq 0\}.$$

The finite element method is based on the variational formulation: find $u \in V$ and $\lambda \in \Lambda$, such that

$$(\nabla u, \nabla v) - \langle \lambda, v \rangle = (f, v) \quad \forall v \in V,$$

and

$$\langle \mu - \lambda, u - g \rangle \geq 0 \quad \forall \mu \in \Lambda.$$

3.1. Discretisation. Let \mathcal{T} denote a finite element mesh consisting of triangular elements $K \in \mathcal{T}$, and $V_{\mathcal{T}} \subset V$, $Q_{\mathcal{T}} \subset Q$ are the corresponding finite element spaces. While in the continuous formulation $\lambda \in H^{-1}(\Omega)$, which is a space of functionals, if we use one of the standard finite element spaces for discretising λ , say elementwise constants, we end up with $\lambda_{\mathcal{T}} \in L^2(\Omega)$. Consequently, we can define the positive part of $Q_{\mathcal{T}}$ as

$$\Lambda_{\mathcal{T}} = \{\mu \in Q_{\mathcal{T}} : \mu \geq 0\} \subset \Lambda$$

and the discrete variational formulation becomes: find $u_{\mathcal{T}} \in V_{\mathcal{T}}$ and $\lambda_{\mathcal{T}} \in \Lambda_{\mathcal{T}}$ such that

$$(9) \quad (\nabla u_{\mathcal{T}}, \nabla v) - (\lambda_{\mathcal{T}}, v) = (f, v) \quad \forall v \in V_{\mathcal{T}},$$

and

$$(10) \quad (\mu - \lambda_{\mathcal{T}}, u_{\mathcal{T}} - g) \geq 0 \quad \forall \mu \in \Lambda_{\mathcal{T}}.$$

Although several stable options exist, we will now fix the finite element spaces to bubble-enriched quadratic space for $u_{\mathcal{T}}$,

$$V_{\mathcal{T}} = \{v \in V : v|_K \in P_2(K) \oplus B_3(K) \quad \forall K \in \mathcal{T}\},$$

and piecewise-constant space for $\lambda_{\mathcal{T}}$,

$$Q_{\mathcal{T}} = \{\mu \in Q : \mu|_K \in P_0(K) \quad \forall K \in \mathcal{T}\},$$

that are part of a family of bubble-enriched mixed methods analysed in Gustafsson–Stenberg–Videman [1]. For this method, we have the following residual a posteriori error estimate which is the fundamental justification behind the adaptive scheme discussed in the upcoming sections:

Theorem 1 (e.g., Gustafsson–Stenberg–Videman [1]). *There exists $C > 0$ such that*

$$\|u - u_{\mathcal{T}}\|_{H^1(\Omega)}^2 + \|\lambda - \lambda_{\mathcal{T}}\|_{H^{-1}(\Omega)}^2 \leq C \sum_{K \in \mathcal{T}} \left\{ \eta_K^2 + \eta_{\partial K}^2 + \eta_{C,K}^2 \right\},$$

where

$$\begin{aligned} \eta_K^2 &= h_K^2 \|\Delta u_{\mathcal{T}} + \lambda_{\mathcal{T}} + f\|_{L^2(K)}^2 \\ \eta_{\partial K}^2 &= \frac{1}{2} h_K \|\llbracket \nabla u_{\mathcal{T}} \cdot n \rrbracket\|_{L^2(\partial K \setminus \partial \Omega)}^2 \\ \eta_{C,K}^2 &= \|(g - u_{\mathcal{T}})_+\|_{H^1(K)}^2 + ((g - u_{\mathcal{T}})_+, \lambda_{\mathcal{T}})_K. \end{aligned}$$

Above n refers to the normal vector and $\llbracket \nabla u_{\mathcal{T}} \cdot n \rrbracket$ refers to the jump of the normal derivative over the element edge. The positive part of $a \in H^1(\Omega)$ is denoted by $(a)_+ = \max(a, 0)$. Furthermore, we have used the following standard notation for the norms in which the discretisation error is being measured:

$$\|w\|_{L^2(S)}^2 = \int_S w^2 dx, \quad \|w\|_{H^1(S)}^2 = \|w\|_{L^2(S)}^2 + \|\nabla w\|_{L^2(S)}^2, \quad S \subset \Omega.$$

The Lagrange multiplier λ belongs, in general, to the dual space of $H_0^1(\Omega)$ which is equipped with the dual norm

$$\|\mu\|_{H^{-1}(\Omega)} = \sup_{\substack{v \in H_0^1(\Omega), \\ \|v\|_{H^1(\Omega)} = 1}} \langle \mu, v \rangle.$$

We note that the dual norm is not directly computable and can be only estimated, e.g., through the mesh-dependent norm

$$\|\mu_{\mathcal{T}}\|_{H^{-1}(\Omega)}^2 \propto \sum_{K \in \mathcal{T}} h_K^2 \|\mu_{\mathcal{T}}\|_{0,K}^2.$$

However, at least in the context of the membrane contact problem (3), it can be intuitively thought of as a measure similar to the total contact force. In particular, the total contact force would be equal to $\langle \mu, 1 \rangle$ while the dual norm maximises the force-like quantity $\langle \mu, v \rangle$ with respect to a normalised weight function $v \in H_0^1(\Omega)$.

3.2. Linearisation. As explained before, inequality-constrained problems are nonlinear due to the unknown Ω_C . We will now present a Newton-type linearisation of (10) which allows finding Ω_C iteratively and efficiently. The second inequality (10) can be written using the L^2 projection, $\pi_{\mathcal{T}} : V_{\mathcal{T}} \rightarrow Q_{\mathcal{T}}$, as

$$(\mu - \lambda_{\mathcal{T}}, \pi_{\mathcal{T}}(u_{\mathcal{T}} - g)) \leq 0 \quad \forall \mu \in \Lambda_{\mathcal{T}},$$

or, after adding and subtracting $\lambda_{\mathcal{T}}$,

$$(\mu - \lambda_{\mathcal{T}}, \lambda_{\mathcal{T}} - \pi_{\mathcal{T}}(u_{\mathcal{T}} - g) - \lambda_{\mathcal{T}}) \leq 0 \quad \forall \mu \in \Lambda_{\mathcal{T}}.$$

This particular form implies that $\lambda_{\mathcal{T}}$ is equal to the orthogonal projection of $\lambda_{\mathcal{T}} - \pi_{\mathcal{T}}(u_{\mathcal{T}} - g)$ onto the set of positive finite element functions $\Lambda_{\mathcal{T}}$.

This statement can be proven as follows: let $R = \lambda_{\mathcal{T}} - \pi_{\mathcal{T}}(u_{\mathcal{T}} - g)$. The above inequality then reads

$$(\lambda_{\mathcal{T}} - \mu, R - \lambda_{\mathcal{T}}) \geq 0 \quad \forall \mu \in \Lambda_{\mathcal{T}}.$$

Applying this and the Cauchy–Schwarz inequality leads to

$$\|R - \lambda_{\mathcal{T}}\|_0^2 = (R - \lambda_{\mathcal{T}}, R - \lambda_{\mathcal{T}}) \leq (R - \mu, R - \lambda_{\mathcal{T}}) \leq \|R - \mu\|_0 \|R - \lambda_{\mathcal{T}}\|_0$$

which holds for every $\mu \in \Lambda_{\mathcal{T}}$. Dividing by $\|R - \lambda_{\mathcal{T}}\|_0$ reveals the definition of an orthogonal projection:

$$\|R - \lambda_{\mathcal{T}}\|_0 \leq \|R - \mu\|_0 \quad \forall \mu \in \Lambda_{\mathcal{T}}.$$

Because $\Lambda_{\mathcal{T}}$ is defined as the set of nonnegative piecewise constant functions, we can write explicitly the orthogonal projection as

$$\lambda_{\mathcal{T}} = (\lambda_{\mathcal{T}} - \pi_{\mathcal{T}}(u_{\mathcal{T}} - g))_+.$$

Furthermore, because $(a)_+$, $a \in \mathbb{R}$, evaluates to a or 0 element-by-element, for each element either

$$(11) \quad \lambda_{\mathcal{T}} = 0 \quad \text{or} \quad \pi_{\mathcal{T}}(u_{\mathcal{T}} - g) = 0.$$

This suggests a solution algorithm where the split (11) is decided by the solution of the previous iteration. Then what remains is to solve a linear problem given by (9) and (11) during each iteration.

As a conclusion, the *primal-dual active set method* for solving the problem (9) and (10) can be written as follows:

- (1) Pick an initial guess for $u_{\mathcal{T}} \in V_{\mathcal{T}}$ and $\lambda_{\mathcal{T}} \in Q_{\mathcal{T}}$.
- (2) Find the set of active elements $\mathcal{A} \subset \mathcal{T}$ such that $\lambda_{\mathcal{T}} - \pi_{\mathcal{T}}(u_{\mathcal{T}} - g)|_K > 0$ for every $K \in \mathcal{A}$.
- (3) Enforce $\lambda_{\mathcal{T}}$ to zero in the complement, i.e. $Q_{\mathcal{A}} = \{\mu \in Q_{\mathcal{T}} : \mu|_K = 0 \ \forall K \in \mathcal{T} \setminus \mathcal{A}\}$.
- (4) Find $u_{\mathcal{T}} \in V_{\mathcal{T}}$ and $\lambda_{\mathcal{T}} \in Q_{\mathcal{A}}$ such that

$$(\nabla u_{\mathcal{T}}, \nabla v) - (\lambda_{\mathcal{T}}, v) - (u_{\mathcal{T}}, \mu) = (f, v) - (g, \mu) \quad \forall (v, \mu) \in V_{\mathcal{T}} \times Q_{\mathcal{A}}.$$

- (5) Check if the iteration has converged by calculating how much $\lambda_{\mathcal{T}}$ changed. If the iteration did not converge, go back to step 2.

The convergence of this iteration is rapid because it is, in fact, a (semismooth) Newton’s method in disguise [25]. In particular, the number of iterations required to converge to any given tolerance (say machine epsilon) is often several order of magnitudes less than in any Uzawa-type fixed point methods we have attempted to use. We have used the relative change in the l^2 -norm of the vector representing $\lambda_{\mathcal{T}}$ as a convergence criterion, see Listing 1 for our Python implementation.

Listing 1: Primal-dual active set method using scikit-fem [26]

```
# to install dependencies: pip install scikit-fem==9.0.0 matplotlib

from skfem import *
from skfem.helpers import *

mesh = MeshTri.init_sqsymmetric().refined(3)
basis = Basis(mesh, ElementTriP0() * ElementTriP2B())

def f(x):
    return 0 * x[0]

def g(x):
    return np.sin(np.pi * x[0]) * np.sin(np.pi * x[1]) - 0.5

@BilinearForm
def bilinf(lam, u, mu, v, _):
    return dot(grad(u), grad(v)) - lam * v - mu * u

@LinearForm
def linf(mu, v, w):
    return f(w.x) * v - g(w.x) * mu

lamu = basis.zeros()
(lam, lambasis), (u, ubasis) = basis.split(lamu)
A = bilinf.assemble(basis)
b = linf.assemble(basis)
G = lambasis.project(g)
res = 1e8

while res > 1e-10:
    (lam, lambasis), (u, ubasis) = basis.split(lamu)
    U = lambasis.project(ubasis.interpolate(u))
    D = np.concatenate((
        basis.get_dofs().all("u^2"),
        basis.get_dofs(elements=np.nonzero(U - G >= lam)[0]).all("u^1"),
    ))
    lamuprev = lamu.copy()
    lamu = solve(*condense(A, b, D=D))
    res = np.linalg.norm(lamu - lamuprev) / np.linalg.norm(lamu)
    print(res)

# to plot: ubasis.plot(u).show()
```

3.3. Implementation. The main ideas behind adaptive finite element schemes are given thoroughly in Verfürth [27]. The theory behind the convergence of the adaptive scheme in case of obstacle problems has been discussed in [28]. We will now briefly summarise the relevant parts on the implementation of adaptive methods for context and to introduce notation. Adaptive finite element methods require:

- (1) an initial mesh \mathcal{T}_0
- (2) an error indicator $E_K = E_K(u_{\mathcal{T}}, \lambda_{\mathcal{T}})$ which can be computed for every element $K \in \mathcal{T}$ given the discrete solution $(u_{\mathcal{T}}, \lambda_{\mathcal{T}}) \in V_{\mathcal{T}} \times A_{\mathcal{T}}$

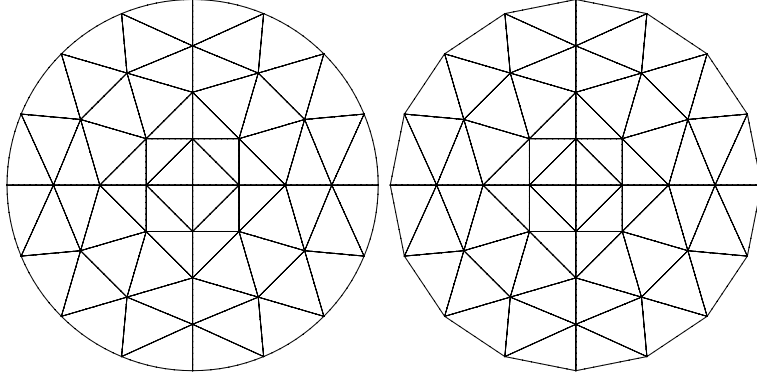


FIGURE 3. Adaptive schemes may overrefine if a curved domain (left) is approximated by a polygonal domain (right) without modifying the error indicator.

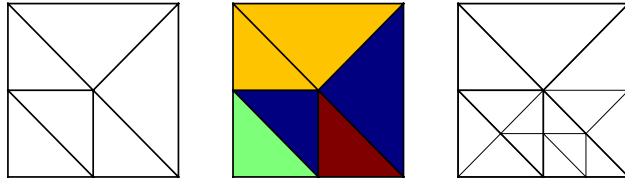


FIGURE 4. (Red-green-blue refinement) The mesh on the left is being refined by marking one triangle for refinement. The red triangle is marked and split into four. To avoid hanging nodes and reduction in the mesh quality, the blue triangles are split into three and the green triangle is split into two. The yellow triangles are not split. The refined mesh is depicted on the right.

- (3) a marking strategy which decides on a subset of elements $\tilde{\mathcal{T}} \subset \mathcal{T}$ to refine based on the values of the error indicator E_K , $K \in \mathcal{T}$
- (4) a mesh refinement algorithm which produces the next mesh \mathcal{T}_{i+1} given a subset of elements to refine on the previous mesh $\tilde{\mathcal{T}}_i \subset \mathcal{T}_i$, $i = 0, 1, \dots$

We wish to note that in adaptive schemes, it is preferable to have an initial mesh \mathcal{T}_0 which accurately represents the geometry of the problem because the estimators may erroneously react to *variational crimes*, e.g., replacing a circular boundary with linear segments (see Figure 3) can cause excess refinement near the boundary while none might be truly required. This is a real fundamental challenge in the practical application of adaptive schemes: for analysis we need to assume some explicit form for the discrete spaces while accurately representing the geometry may require higher order mappings and, hence, different finite element spaces that may or may not warrant for a new analysis using different estimators. For now we assume that the domain Ω can be specified exactly by a triangular mesh.

It is beneficial to have an initial mesh \mathcal{T}_0 which consist of shape-regular elements. While this can be avoided using mesh smoothing, performing refinement without smoothing is useful because this leads to a sequence of meshes

$$\mathcal{T}_0 \supset \mathcal{T}_1 \supset \mathcal{T}_2 \supset \dots$$

where every element in the previous mesh \mathcal{T}_i is a union of smaller or equal elements in the subsequent mesh \mathcal{T}_{i+1} . Consequently, the converged solution on \mathcal{T}_i can be interpolated on \mathcal{T}_{i+1} without much difficulty and computational effort to obtain an initial guess for the next primal-dual iteration. Use of an initial guess from the previous mesh will greatly reduce the number of iterations required for the primal-dual iteration to converge; see, e.g., Figure 5.

After calculating the discrete solution corresponding to the mesh \mathcal{T}_i , we evaluate the error indicator on each element $K \in \mathcal{T}_i$:

$$(12) \quad E_K = \sqrt{\eta_K^2 + \eta_{\partial K}^2 + \eta_{C,K}^2}.$$

Next we decide which elements to refine based on a marking strategy, referred to as *maximum strategy* in Verfürth [27], which marks $K \in \mathcal{T}_i$ for refinement if it is larger than some given parameter $\beta \in (0, 1)$ times the largest error indicator:

$$\tilde{\mathcal{T}}_i = \left\{ K \in \mathcal{T}_i : E_K \geq \beta \max_{K' \in \mathcal{T}_i} E_{K'} \right\}.$$

The parameter β is used to control how many elements are refined during each iteration of the adaptive scheme – larger values may lead to better final meshes and lower error (in absolute terms) but this also drastically increases the number of linear solves. For simplicity, we have set $\beta = \frac{1}{2}$ which, according to Verfürth [27], is a popular and well-established choice. In practice, we have observed that changing β does not seem to affect the asymptotic convergence rate.

Finally, we split the marked triangles using a mesh refinement algorithm, referred to as *regular red refinement* or *red-green-blue refinement*, which produces \mathcal{T}_{i+1} given $\tilde{\mathcal{T}}_i$. The main idea is to split each triangle in $\tilde{\mathcal{T}}_i$ into four while the neighboring elements are split into two or three triangles depending on the lengths of the edges, to avoid hanging nodes and element quality reduction; see Figure 4 for an example of the mesh refinement algorithm applied to a tiny mesh. See Listing 2 for our Python implementation of the adaptive refinement.

Listing 2: Evaluate error estimators using scikit-fem [26]

```
# before use: run the solver from above

gradbasis = basis.with_element(ElementDG(ElementTriP3()))
ux = gradbasis.project(ubasis.interpolate(u).grad[0])
uy = gradbasis.project(ubasis.interpolate(u).grad[1])

@Functional
def interior(w):
    return w.h ** 2 * (w["ux"].grad[0] + w["uy"].grad[1]
                      + w["lam"] + f(w.x)) ** 2

eta_int = interior.elemental(gradbasis, ux=ux, uy=uy,
                             lam=lambasis.interpolate(lam))

fbasis = [InteriorFacetBasis(mesh, ElementTriP2B(), side=i)
           for i in [0, 1]]
u12 = {"u{}".format(i + 1): fbasis[i].interpolate(u) for i in [0, 1]}

@Functional
def edge_jump(w):
    return w.h * dot(grad(w["u1"]) - grad(w["u2"]), w.n) ** 2

eta_edge = edge_jump.elemental(fbasis[0], **u12)
tmp = np.zeros(mesh.facets.shape[1])
np.add.at(tmp, fbasis[0].find, eta_edge)
eta_edge = np.sum(.5 * tmp[mesh.t2f], axis=0)

def gx(x):
    return np.pi * np.cos(np.pi * x[0]) * np.sin(np.pi * x[1])

def gy(x):
    return np.pi * np.sin(np.pi * x[0]) * np.cos(np.pi * x[1])

@Functional
def contact(w):
    ind = np.maximum(g(w.x) - w["u"], 0)
    return ind * (np.maximum(g(w.x) - w["u"], 0)
                 + gx(w.x) - w["u"].grad[0]
                 + gy(w.x) - w["u"].grad[1]
                 + w["lam"])

eta_contact = contact.elemental(basis,
                                u=ubasis.interpolate(u),
                                lam=lambasis.interpolate(lam))

eta = eta_int + eta_edge + eta_contact

# to plot: mesh.plot(eta).show()
# to refine: mesh.refined(adaptive_theta(eta)).draw().show()
```

4. COMPUTATIONAL DEMONSTRATIONS

The following numerical results were created using scikit-fem [26] which relies heavily on Python scientific computing ecosystem [29, 30, 31]. All results are obtained using minor variations of the source code in Listings 1 and 2. The mesh generation for the torsion example was done using a variant of distmesh [32].

4.1. Membrane contact problem. We will start with an academic example of a membrane contact problem, i.e. we solve (3) with $\Omega = (0, 1) \times (0, 1)$, $f = 0$, and $G = 1$. The obstacle is given by

$$g = g(x, y) = \sin \pi x \sin \pi y - \frac{1}{2}.$$

The resulting sequence of error indicators and adaptive meshes are given in Figure 6 and Figure 9. The solutions are given in Figure 10 and Figure 11.

We observe that the contact boundary is – while not exactly a circle – circular in shape which is a consequence of the symmetry of g with respect to the axes $x = \frac{1}{2}$ and $y = \frac{1}{2}$. The error indicators in Figure 6 show that depending on the iteration, different parts of the error indicator are active and, hence, responsible for the refinement of particular areas within the computational domain. For instance, it becomes clear that $\eta_{C,K}$ is mainly responsible for refinement within and on the boundary of the coincidence set Ω_C while $\eta_{\partial K}$ is more active outside of Ω_C .

The shape of the coincidence set is clearly visible in the contact force, Figure 10, whose approximation is visually improved by the use of adaptive meshing. The discrete solution $u_{\mathcal{T}_5}$ corresponding to the fifth mesh is given in Figure 11. The best approach for observing the convergence of the adaptive iteration is to plot the sum of the error indicators as a function of the degrees-of-freedom N , see Figure 12 which also compares the result between adaptive and uniform mesh sequences. Based on the a posteriori error estimate, Theorem 1, the sum of error indicators gives an upper bound for the total error. For the adaptive mesh sequence, we can expect the total error to always converge at a rate which derives directly from the polynomial degree of the finite element spaces while the uniform mesh sequence remains limited by the regularity of the loading, the boundary data or the shape of the computational domain.

For quadratic finite element basis and two-dimensional smooth problems the error is $\mathcal{O}(N^{-1})$. For the uniform mesh sequence the error is $\mathcal{O}(N^{-\alpha})$ where $\alpha > 0$ may have any value less or equal to 1 depending on the problem setup while the adaptive scheme recovers the rate $\mathcal{O}(N^{-1})$ irrespective of the smoothness of the loading, boundary data or the shape of the boundary. In addition to possible improvements in the asymptotic rates, we usually observe a clear improvement in the absolute error. For example, based on the rightmost data points in Figure 12, we can obtain the same discretisation error with almost 75% reduction in the number of degrees-of-freedom.

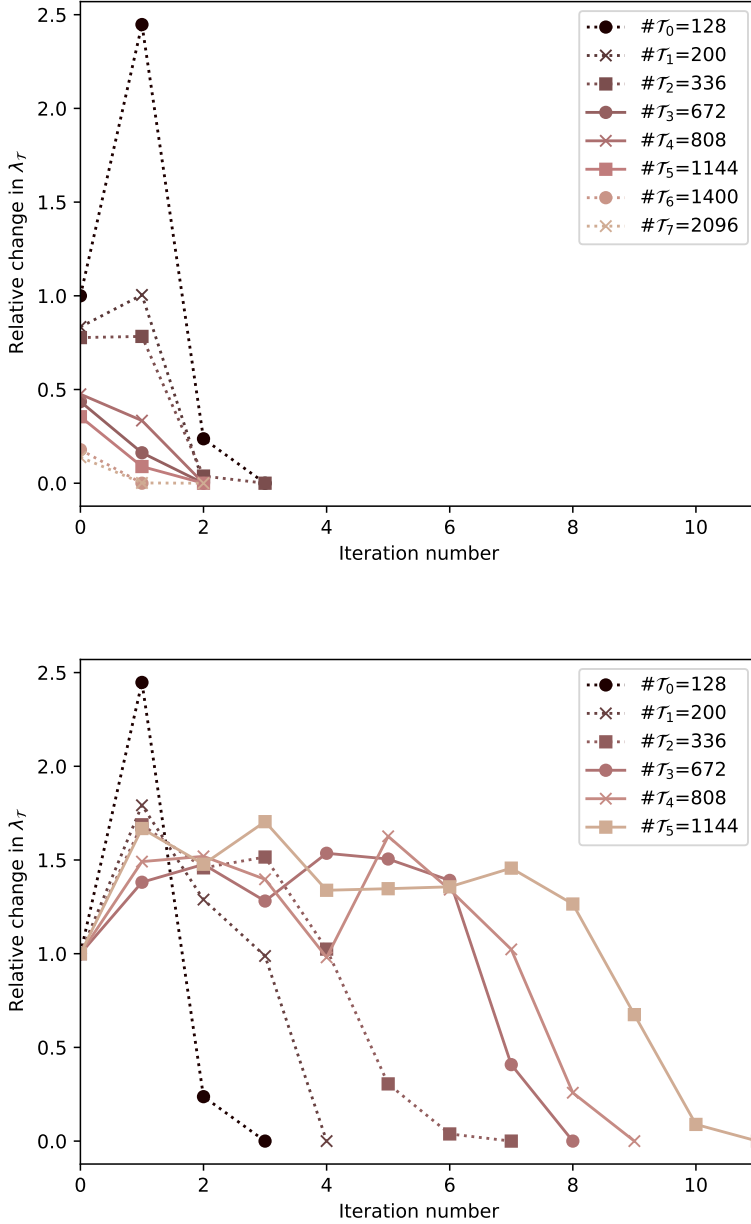


FIGURE 5. (Primal-dual active set method) The iterations required for the primal-dual active set method to converge can be reduced significantly by projecting the previous solution to the refined mesh (top) versus starting from a zero initial guess (bottom).

4.2. Plastic torsion of I beam. Next we consider the torsion of a steel I beam with standard European IPN 80 profile. The cross section boundary is modelled using distance fields which can be used both for mesh generation [32] and for defining δ in the formulation (5). The distance field and the initial mesh are depicted in Figure 13. The parameters of the problem are fixed in Table 1 and the twist per unit length θ is calculated as

$$\theta = \frac{2\pi\gamma}{180^\circ l}.$$

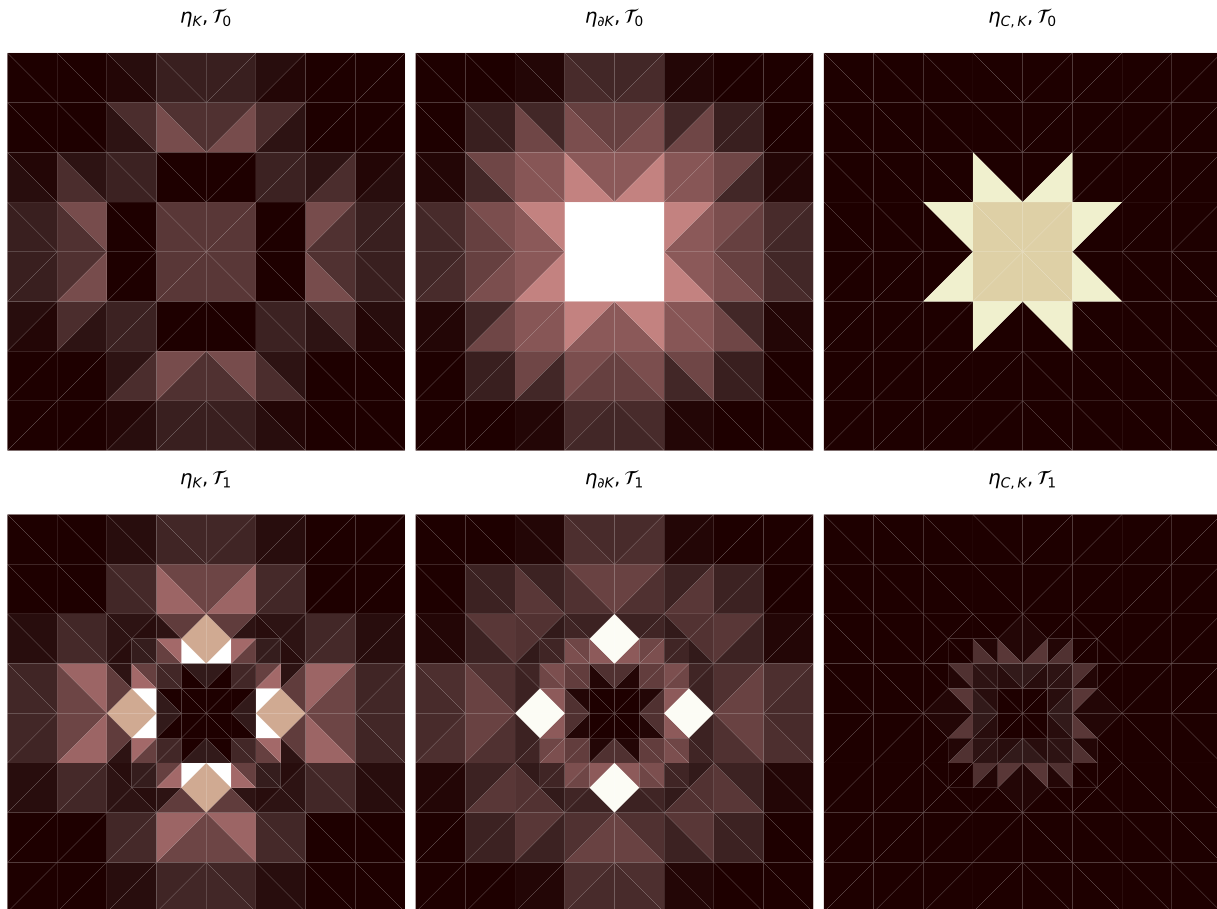


FIGURE 6. (The sequence of error indicators for the membrane problem, part 1/3) The same colourmap is used for each indicator. Their exact values are of no importance as the mesh refinement is driven by their relative differences. In particular, elements within a 50 % difference of the maximum value are split during each iteration.

TABLE 1. Parameters of the plastic torsion problem.

<i>parameter (symbol)</i>	<i>value (unit)</i>
shear modulus (G)	79.3 (GPa)
yield stress (τ)	0.240 (GPa)
angle of twist (γ)	8 ($^\circ$)
length of the beam (l)	400 (mm)

This problem is modelled after the experimental setup in Boru [33] which allows verifying that the plastic deformation occurs roughly at the same angle of twist as in the experimental setup.

This is a challenging problem for the adaptive scheme because parts of the domain boundary consist of circle arcs. Consequently, we have implemented the following changes to the basic adaptive scheme:

- (1) The mesh uses quadratic isoparametric mapping to approximate the domain boundary using piecewise quadratic segments (see Figure 14)
- (2) The mesh refinement algorithm uses the distance field of Figure 13 to project any new mesh nodes onto the boundary
- (3) Laplacian mesh smoothing is applied after each refinement step.

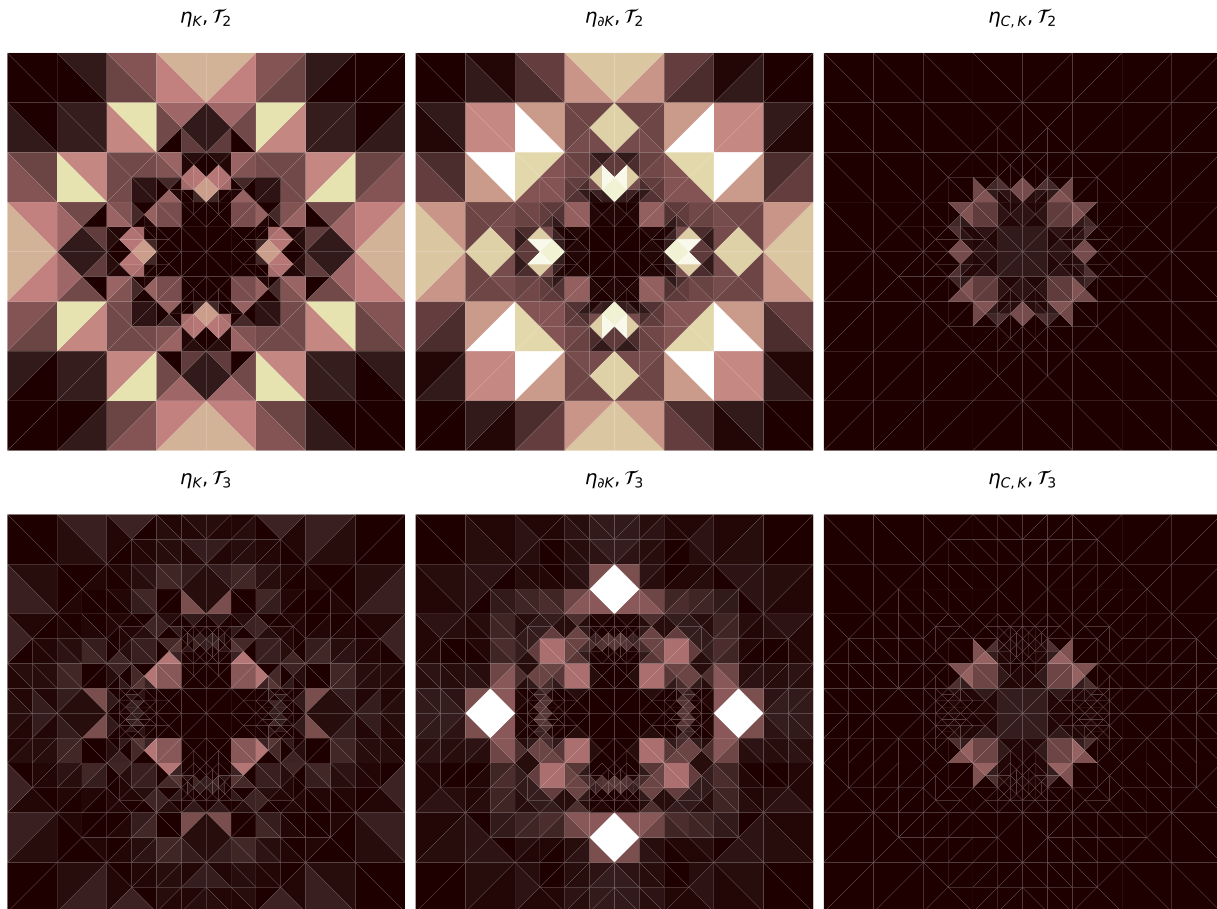


FIGURE 7. (The sequence of error indicators for the membrane problem, part 2/3)

The purpose of the change 1 is to minimise the effect of the variational crime due to inexact boundary representation. It is not possible to completely remove this effect using a piecewise polynomial mapping because circles cannot be represented exactly by polynomials – the consequence of which is exemplified by the sequence of meshes in Figure 16 and Figure 17 with some obvious refinement also near the end of the flanges consisting of outer circular arcs. Fortunately, the adaptive scheme is clearly not stuck on refining a single part of the domain only which would be the case if linear boundary segments were used.

The change 2 is also essential and might be challenging to implement for arbitrary domains and meshes. However, as our domain is already defined using the distance field δ , it becomes a simple evaluation of the distance field at the locations of the new nodes and moving them in the direction of the normal vector. The change 3 is optional but retaining mesh regularity in the red-green-blue refinement requires, in general, checking how many times each edge has been split and changing the refinement type from green to blue accordingly. This may in some cases lead to a blow-up of the refinement zone size [27, p. 68] and, hence, we avoid changing the refinement type and instead use Laplacian smoothing to improve mesh regularity.

We note that the use of mesh smoothing will make it difficult and computationally more demanding to reuse the solution as an initial guess. In particular, the projection between nonmatching meshes requires finding intersections of the triangles for constructing integration points and calculating L^2 projection from one mesh to another. After this implementational challenge is solved, we are able to again bound the number of primal-dual iterations by a small constant, see Figure 15. The first 18 solutions from the sequence of Lagrange multipliers are given in Figure 18 and Figure 19, and a close-up view of the plastic zones corresponding to the final solution is given in Figure 20. While the initial mesh does not distinguish between

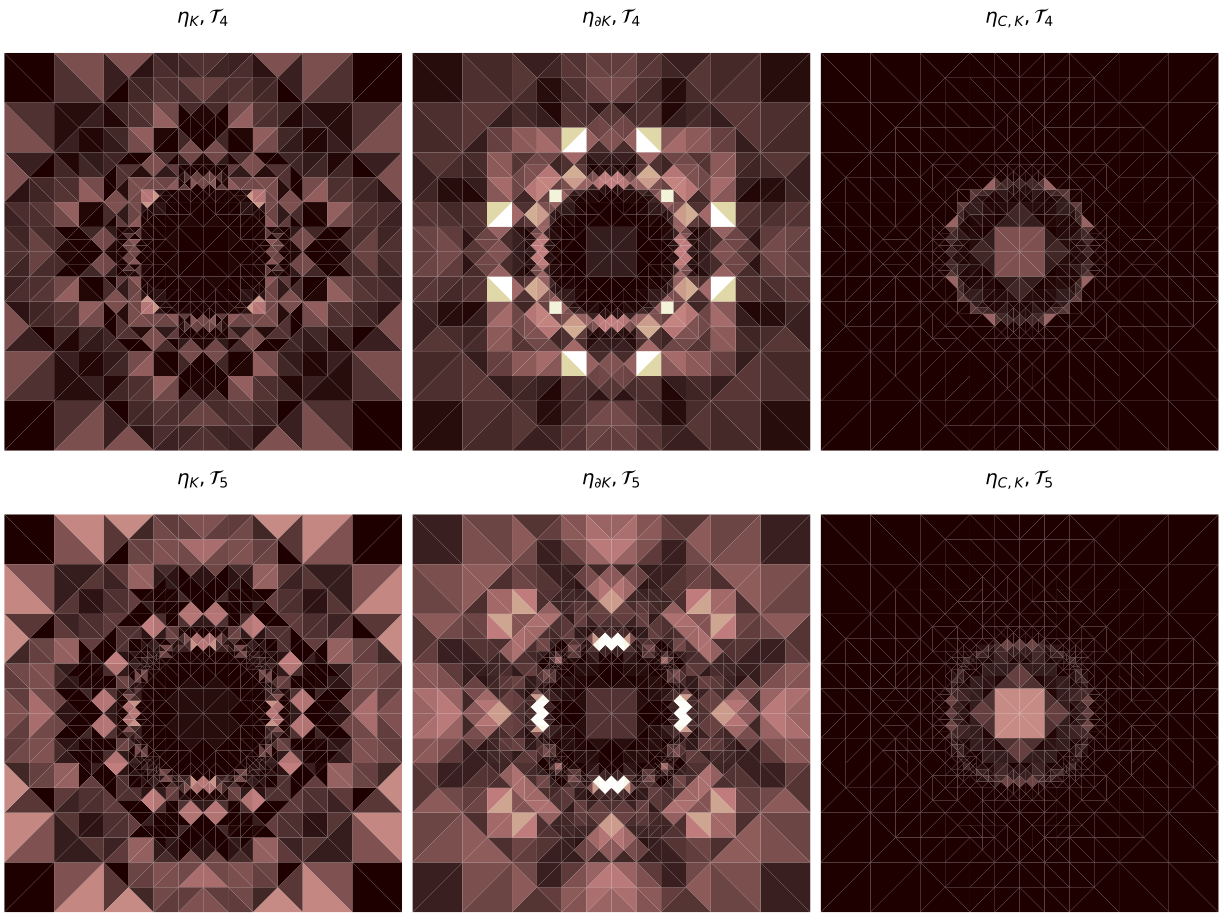


FIGURE 8. (The sequence of error indicators for the membrane problem, part 3/3)

the different plastic zones, the different zones are clearly visible in the final solution. The convergence is again tracked using the sum of the error indicators, given in Figure 21.

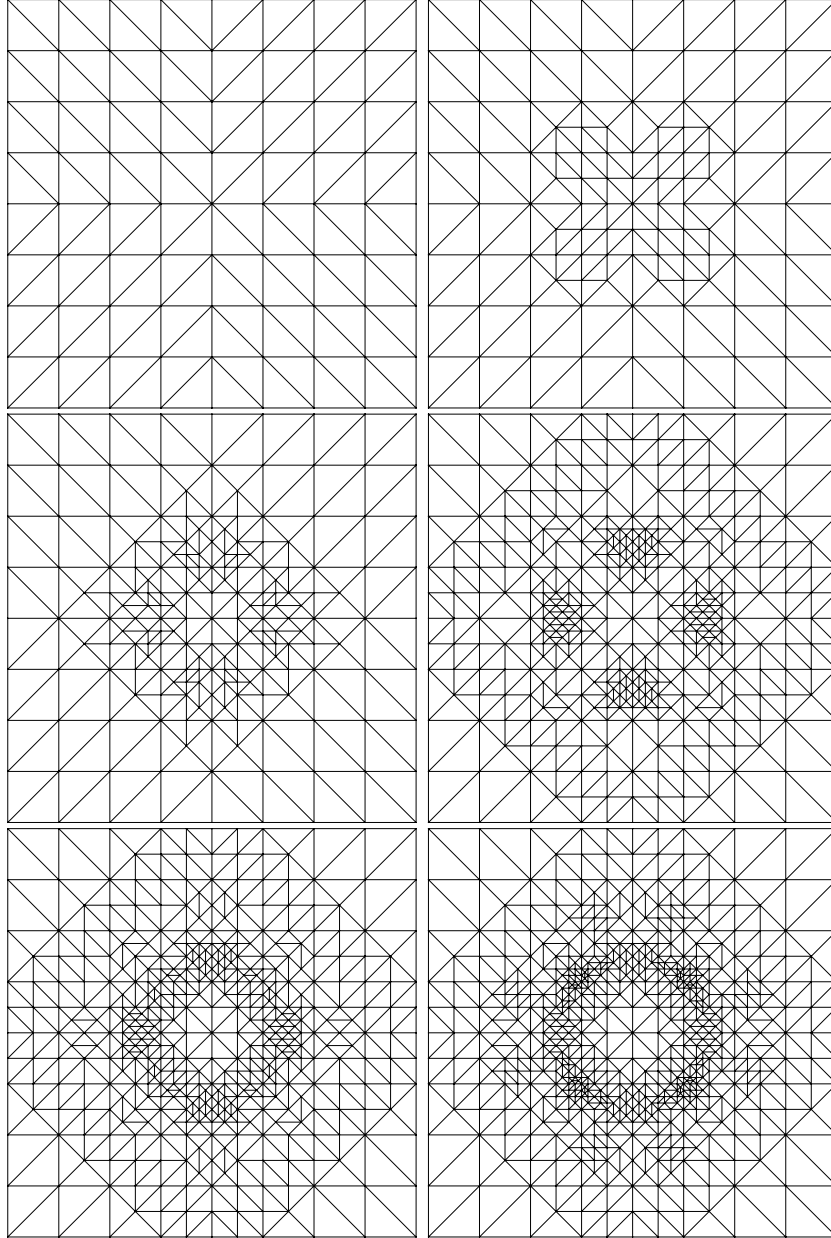


FIGURE 9. (The sequence of adaptive meshes for the membrane problem)

4.3. Cavitation in a hydrodynamic bearing. As a final computational demonstration, we consider the lubricant pressure in a hydrodynamic bearing. The problem is modelled after the experimental setup presented in Etsion–Ludwig [34] and applied further in Braun–Hendricks [35], see Table 2 for the parameters we have used in the simulation. We note that the lubricant viscosity is highly dependent on the temperature of the lubricant and that the temperature is not constant within the bearing [34]. However, based on the measurement data, it becomes obvious that the bearing rotational speed and the lubricant temperature have a correlation [35]. This can be explained by the fact that higher rotational speeds lead to higher shear rates and, hence, higher viscous heating within the lubricant.

Consequently, the experimental maximum pressure [35] is not linearly proportional to the surface velocity V , as one would expect based on the right hand side of (6), since the temperature is inversely proportional to

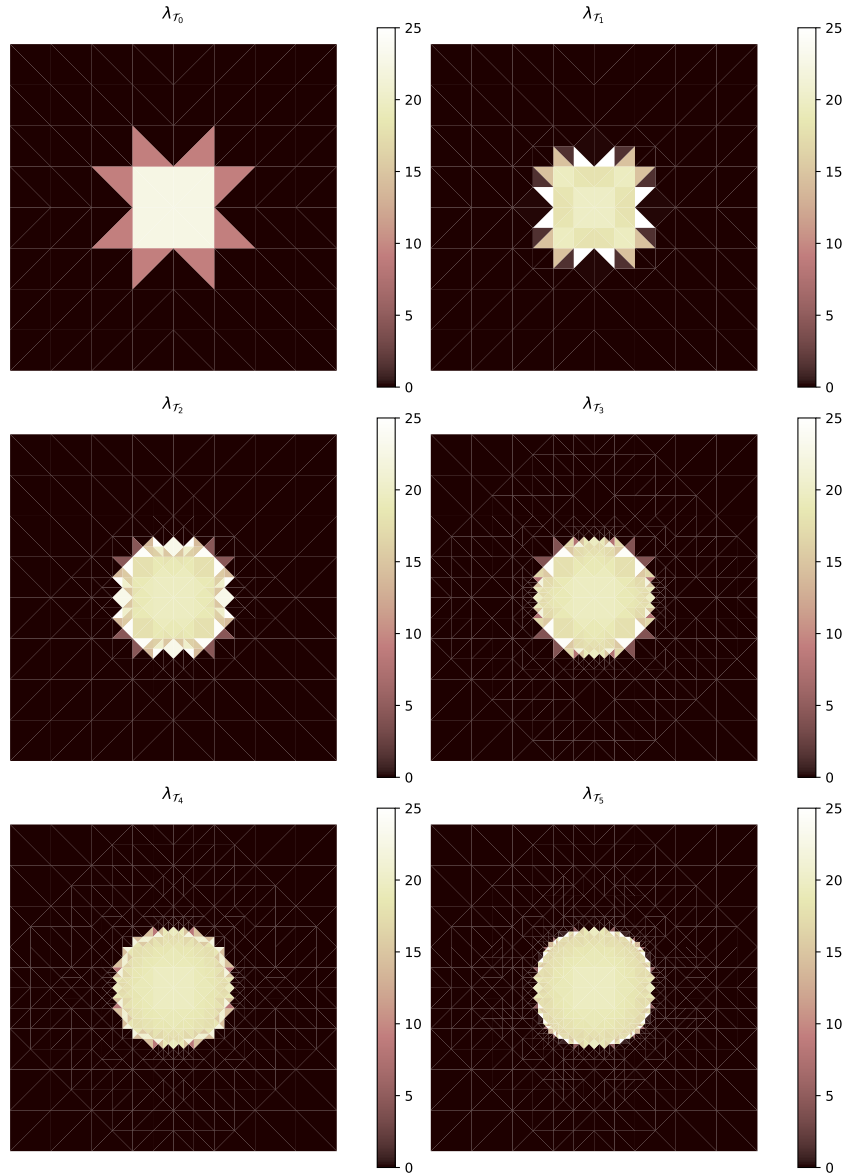


FIGURE 10. The sequence of Lagrange multipliers for the membrane problem.

the viscosity of the lubricant μ . There exist separate models for thermohydrodynamics that could be utilised for studying the effect of the nonzero temperature gradient; see, e.g., Feng et al. [36]. On the other hand, we could technically use the temperature measurement data presented in Braun–Hendricks [35] to calculate a space-dependent value for the dynamic viscosity and use that value in our simulation. For simplicity, we choose a representative constant value for μ which is close to the true viscosity at the measured maximum temperature 33°C while the measured minimum temperature is approximately 22°C . The cavitation pressure is a rough approximation of the minimum pressure in the pressure diagrams of [35]. We note that this problem setup can reasonably reproduce the experimental pressure at the midline, see Figure 22 for a comparison.

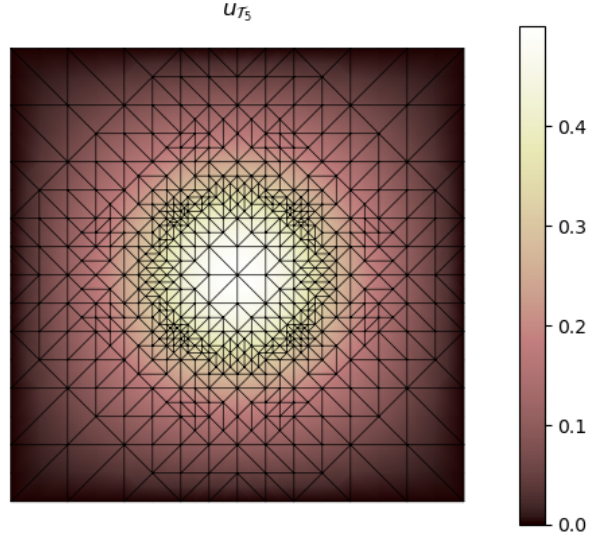


FIGURE 11. The displacement of the membrane.

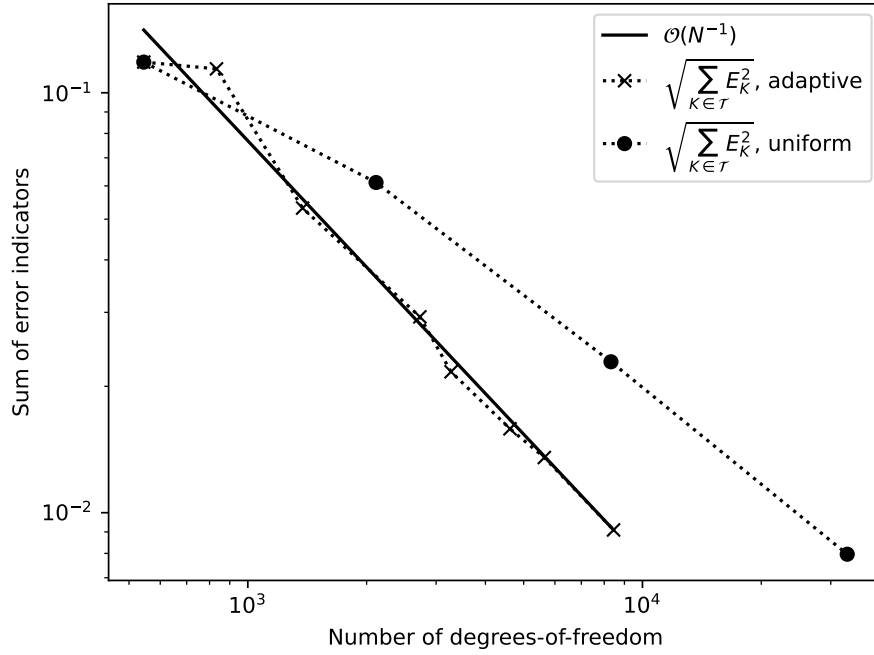


FIGURE 12. The sum of the error indicators for the membrane problem.

We do the following changes to the error indicator to account for the large variations of d^3 within the computational domain [3]:

$$\eta_K^2 = \frac{h_K^2}{d_K^3} \|\nabla \cdot (\frac{d^3}{\mu} \nabla p_{\mathcal{T}}) + \lambda_{\mathcal{T}} + f\|_{L^2(K)}^2$$

$$\eta_{\partial K}^2 = \frac{1}{2} \frac{h_K}{d_K^3} \|\frac{d^3}{\mu} [\nabla p_{\mathcal{T}} \cdot n]\|_{L^2(\partial K \setminus \partial \Omega)}^2,$$

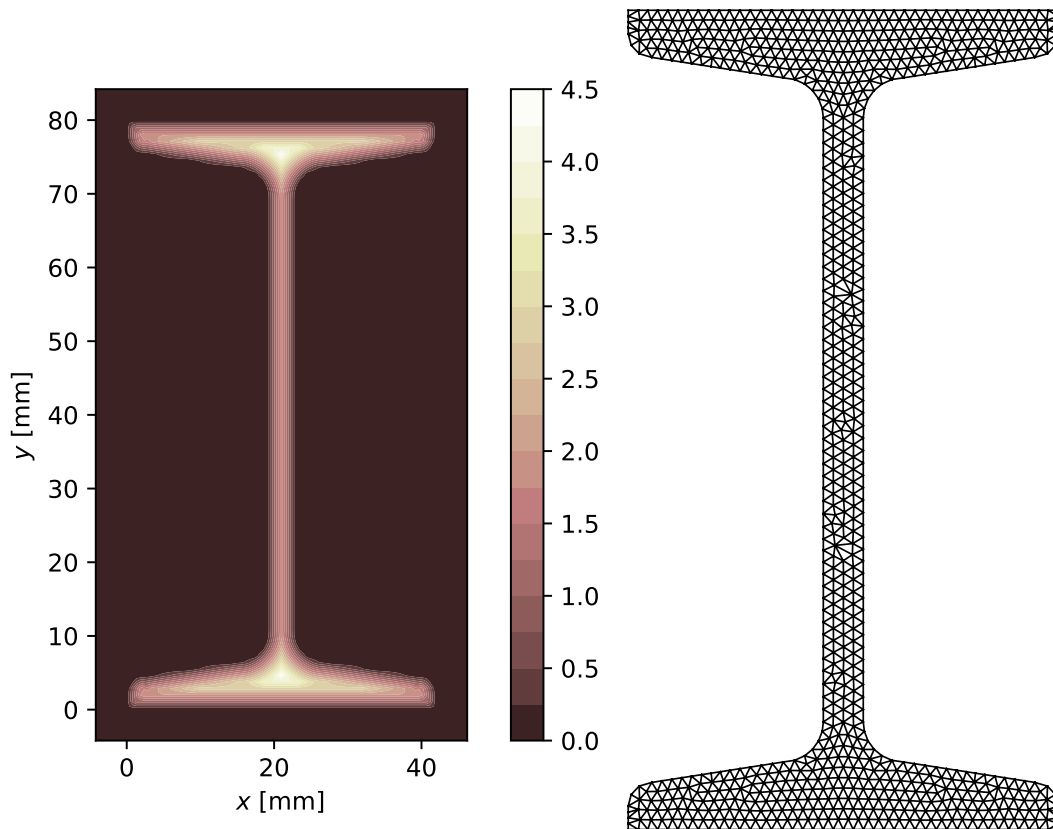


FIGURE 13. The distance field for the IPN 80 profile and the initial mesh.

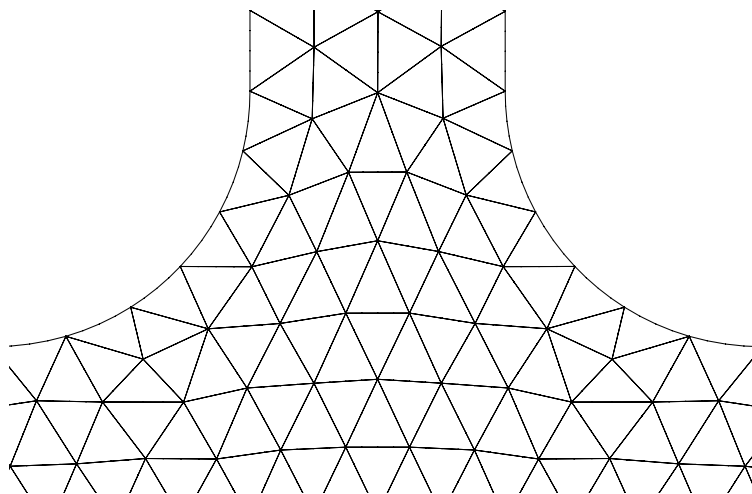


FIGURE 14. A close-up view of the quadratic initial mesh.

where d_K is the mean value of d within the triangle K . The sequence of adaptive meshes in Figure 23 shows that it is important, in terms of discretisation error, to triangulate accurately the boundary of the cavitation zone Ω_C . We can observe the shape of the cavitation zone in Figure 24 and it has a distinctive shape, reminiscent of the photographs taken of the experimental setup with transparent bearing surfaces [35]. The

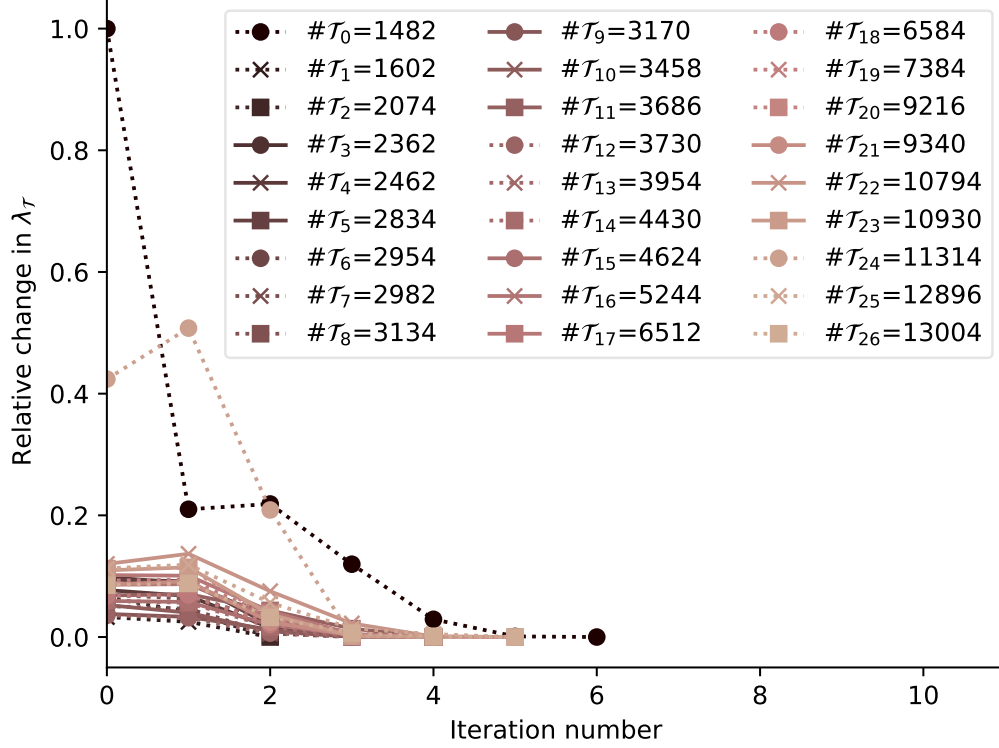


FIGURE 15. Primal-dual active set method.

TABLE 2. Parameters of the hydrodynamic bearing problem.

<i>parameter (symbol)</i>	<i>value (unit)</i>	<i>explanation</i>
radius of the bearing (R)	25.4 (mm)	from [35]
length of the bearing (L)	38.1 (mm)	from [35]
bearing clearance (c_1)	114 (μm)	from [34]
dynamic viscosity at $T = 20^\circ\text{C}$ ($\mu_{20^\circ\text{C}}$)	0.0456 (Pa·s)	from [35]
dynamic viscosity at $T = 40^\circ\text{C}$ ($\mu_{40^\circ\text{C}}$)	0.0232 (Pa·s)	from [35]
dynamic viscosity (μ)	0.0307 (Pa·s)	$\mu_{20^\circ\text{C}} < \mu < \mu_{40^\circ\text{C}}$
eccentricity (e)	0.4 (1)	from [35]
oil bath pressure (p_{env})	172 (kPa)	from [35]
cavitation pressure (p_{cav})	100 (kPa)	pressure diagrams in [35]
speed (V)	5.320 (m/s)	≈ 2000 RPM [35]

pressure over the full journal bearing is given in Figure 25 and the observed numerical convergence rate is depicted in Figure 26.

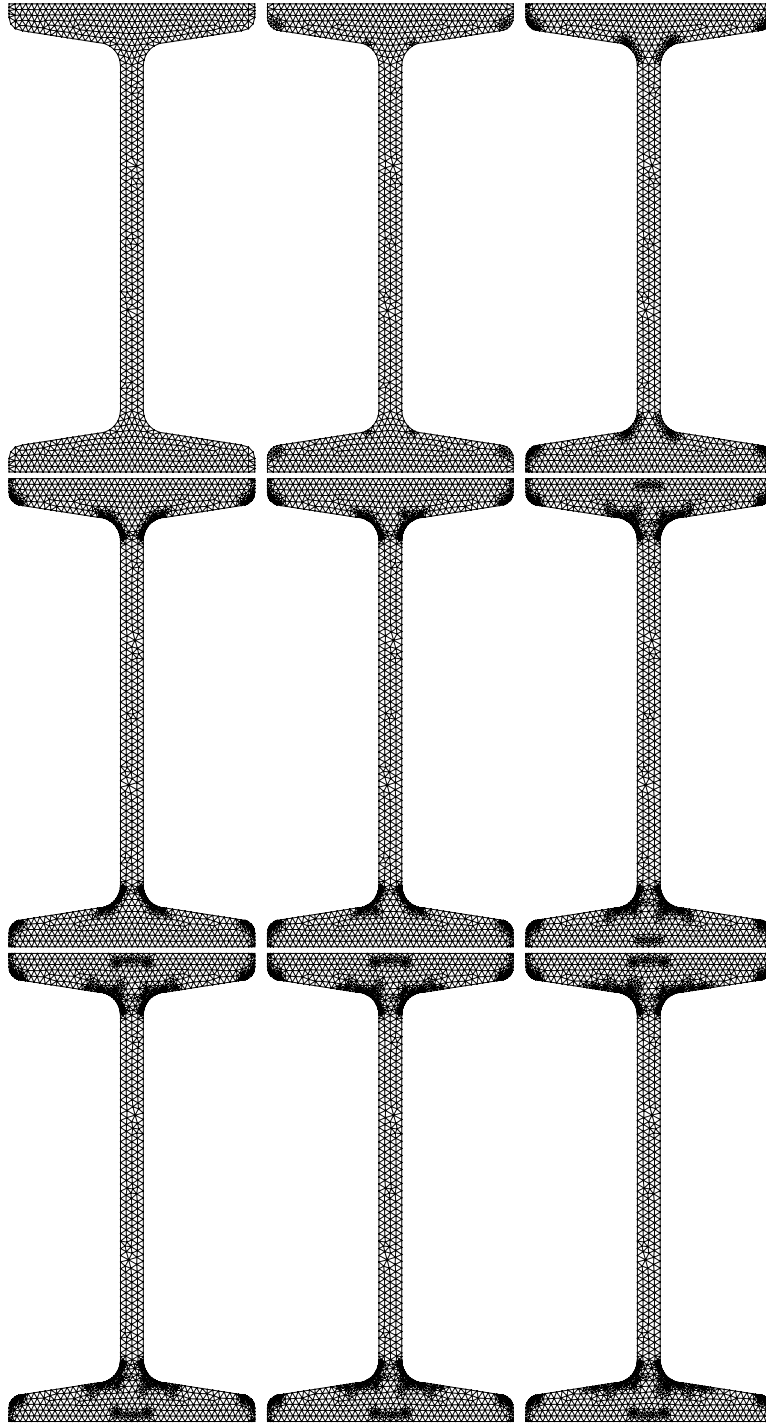


FIGURE 16. The sequence of meshes for the torsion problem, part 1/2.

5. DISCUSSION

Adaptive finite elements use less degrees-of-freedom to achieve a given level of accuracy. Hence, they allow increasing the limit of complexity before supercomputing is required while simultaneously reducing the user time spent on meshing. This is also true for inequality-constrained problems, such as the obstacle problems

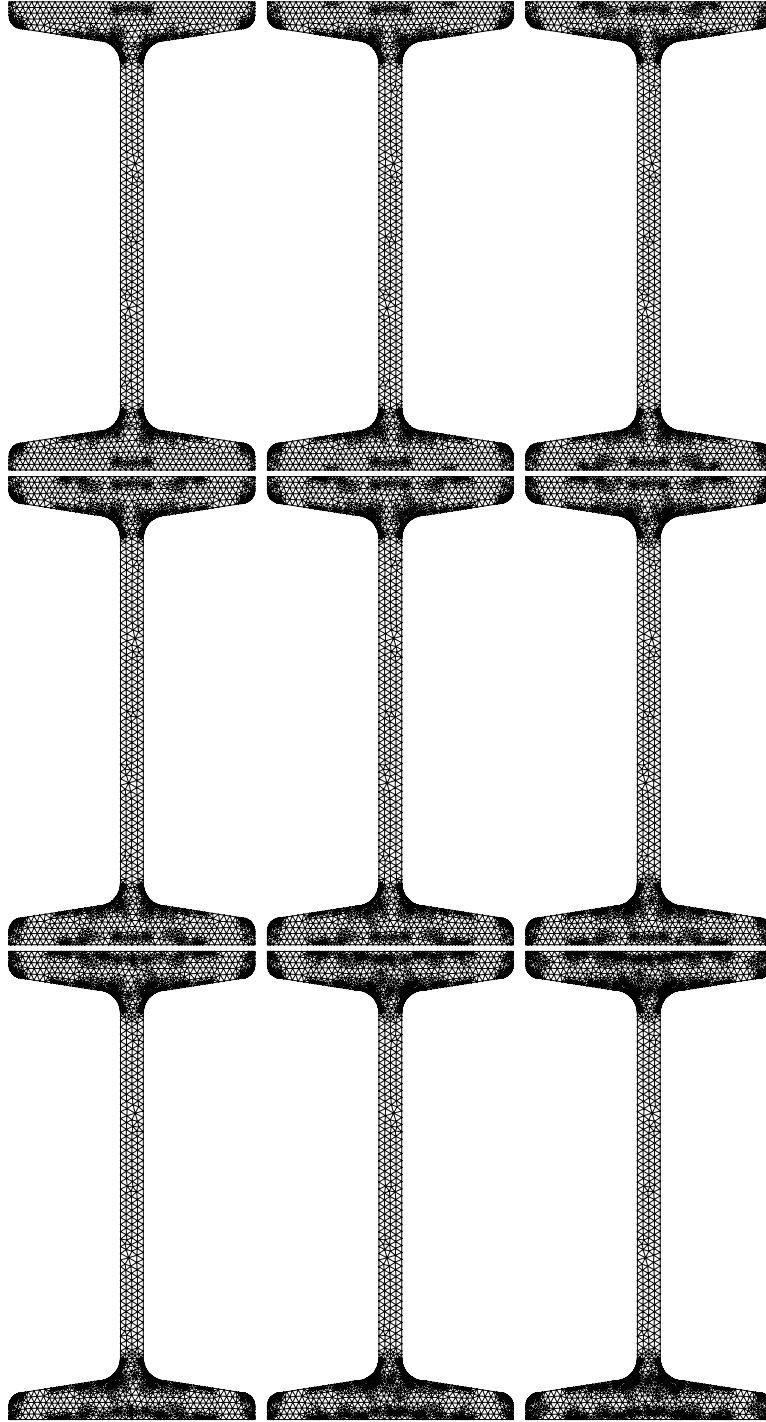


FIGURE 17. The sequence of meshes for the torsion problem, part 2/2.

presented in this chapter, or even more general elastic contact problems [7]. For example, it is clear that the location of the coincidence set may change in time-dependent problems and no fixed mesh can be ideal over the entire time range.

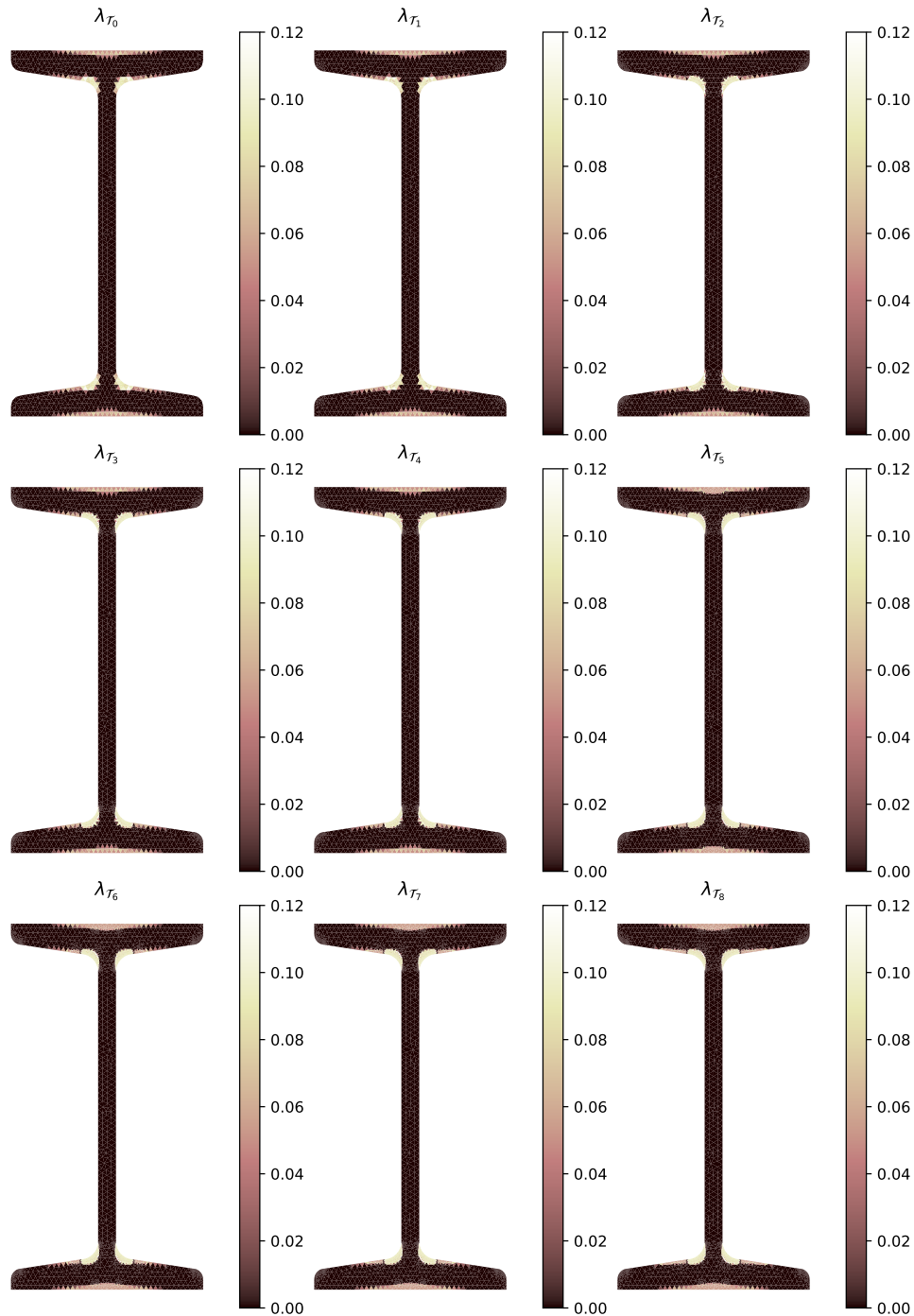


FIGURE 18. The sequence of Lagrange multipliers for the torsion problem, part 1/2.

On the other hand, there are general challenges related to the practical adoption of adaptive methods including but not limited to: (1) the estimators are specific to a particular continuous problem and its discretisation, and different problems require different estimators which means that the continuous formulation and its relation to the discretisation must be well understood; (2) nonpolygonal domains can be challenging or impossible to represent exactly using standard finite elements while a description of the exact geometry must be available to the refinement algorithm; and (3) different norms may be preferable, e.g., due to large

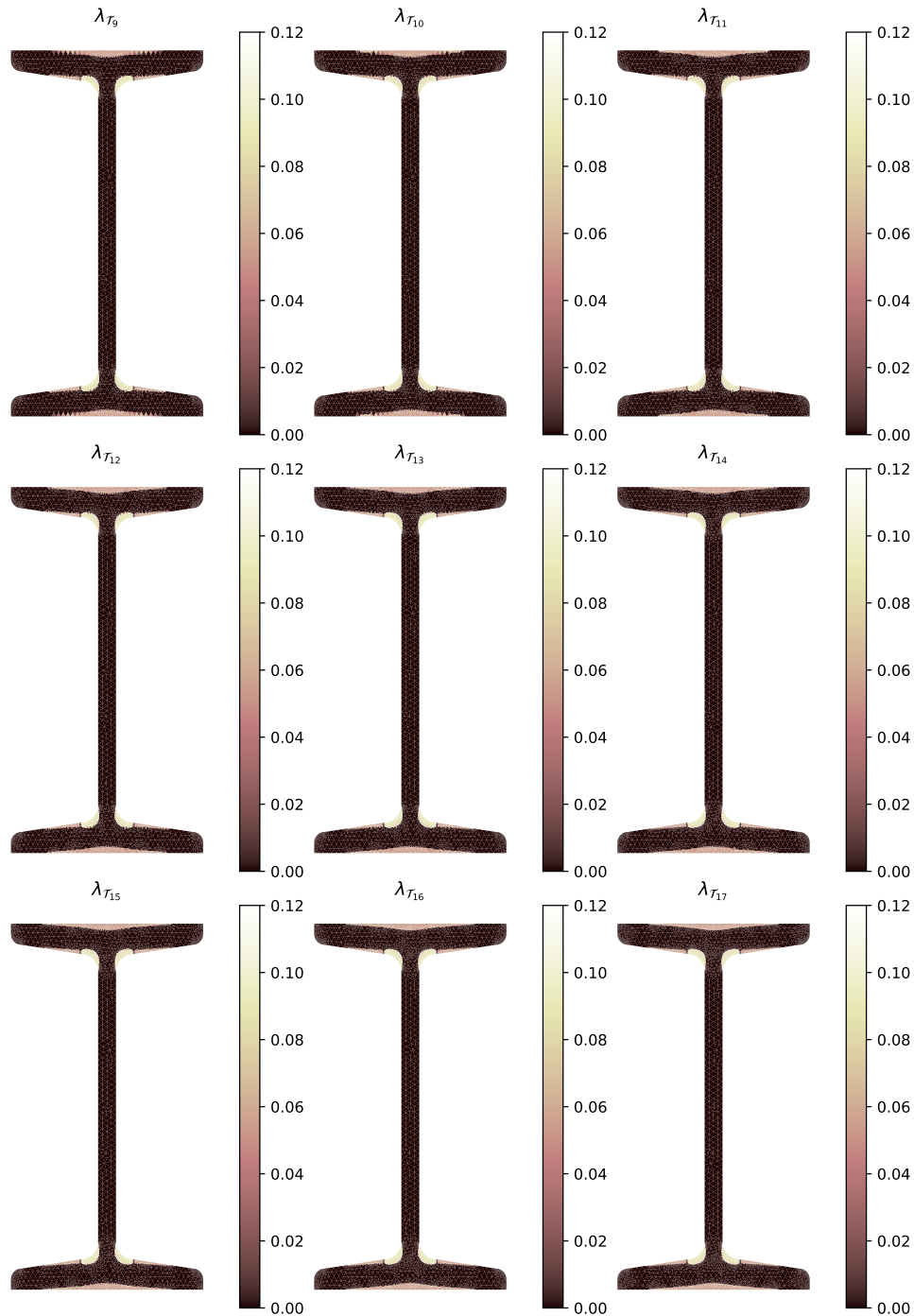


FIGURE 19. The sequence of Lagrange multipliers for the torsion problem, part 2/2.

variations in the material parameters or loadings, or simply due to the preferences of the user, that again lead to different error estimators.

The computational demonstrations presented in this chapter exemplify some of the aforementioned challenges. Many popular finite element solvers for day-to-day engineering use fixed meshes and do not integrate geometry description, as would be required to overcome challenge (2). Solving challenges (1) and (3) in an automatic manner would require an extensive catalogue of estimators for various governing equations,

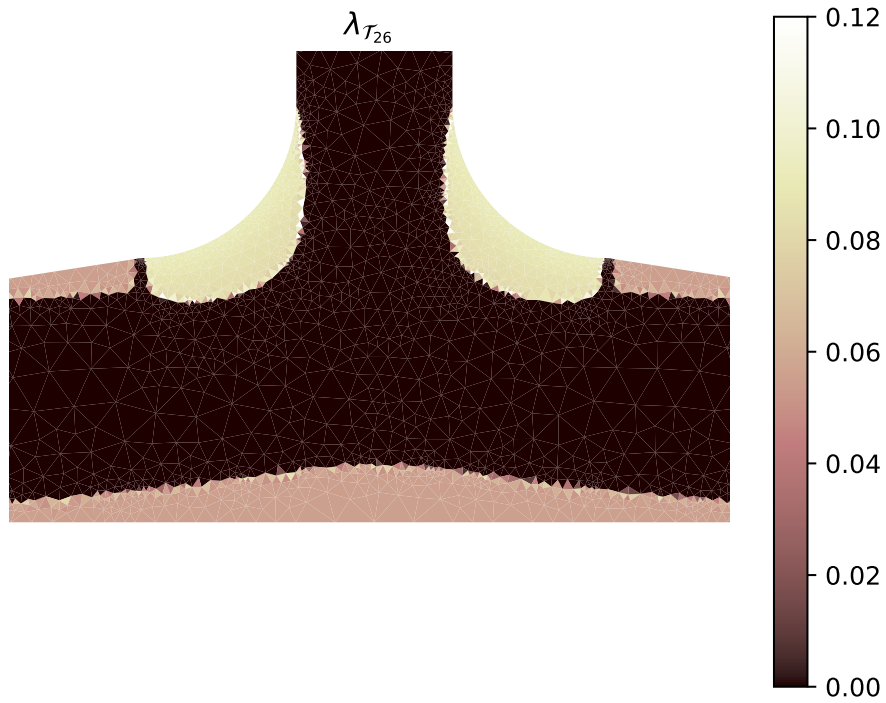


FIGURE 20. A close-up view of the Lagrange multiplier.

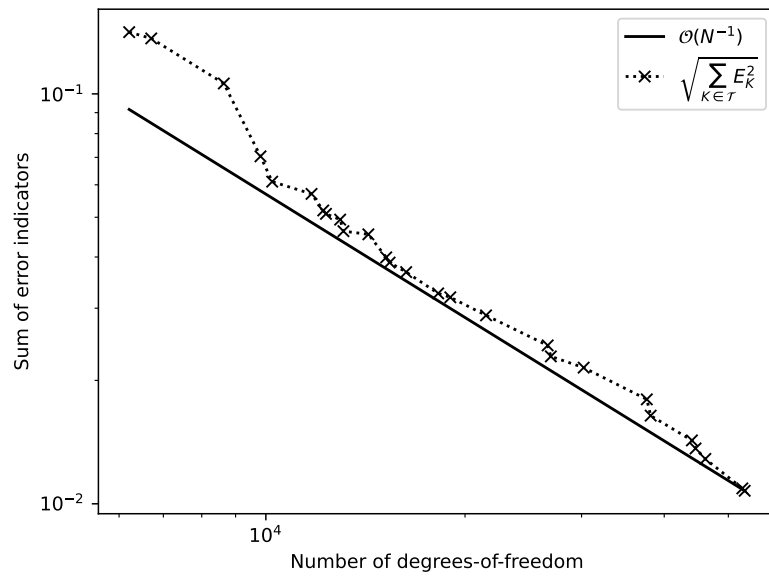


FIGURE 21. The sum of the error indicators for the torsion problem.

boundary conditions, material fields, and finite element methods. For other problems of practical interest, such as curved boundary, two body, or large displacement problems in frictional contact [37, 38, 8, 39], the a posteriori error analysis may not be developed enough so that reliable adaptive schemes can be established.

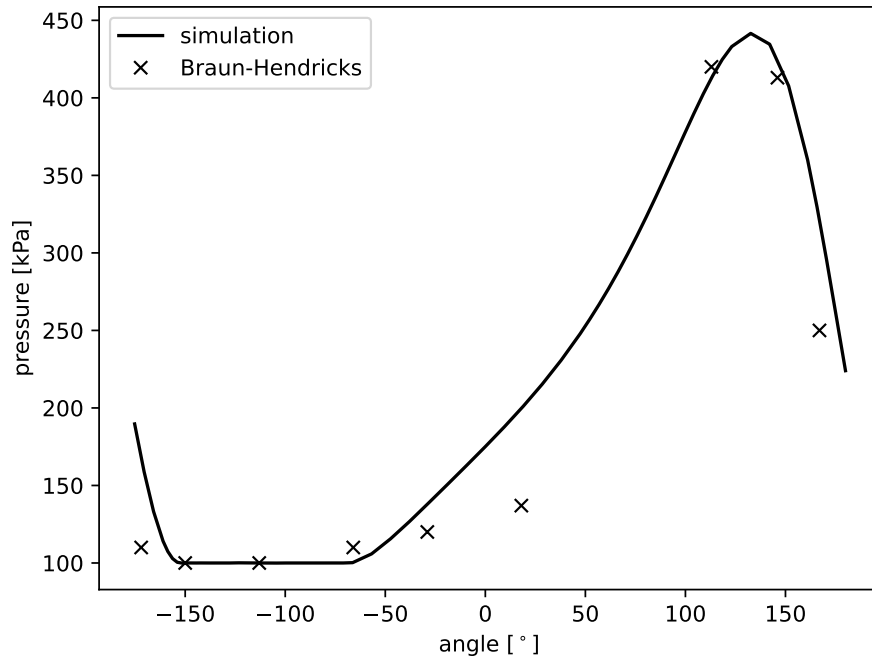


FIGURE 22. (The pressure at the midline) A comparison is done against a few experimental data points from Braun-Hendricks [35] which contains the measured pressure distribution over the entire bearing surface.

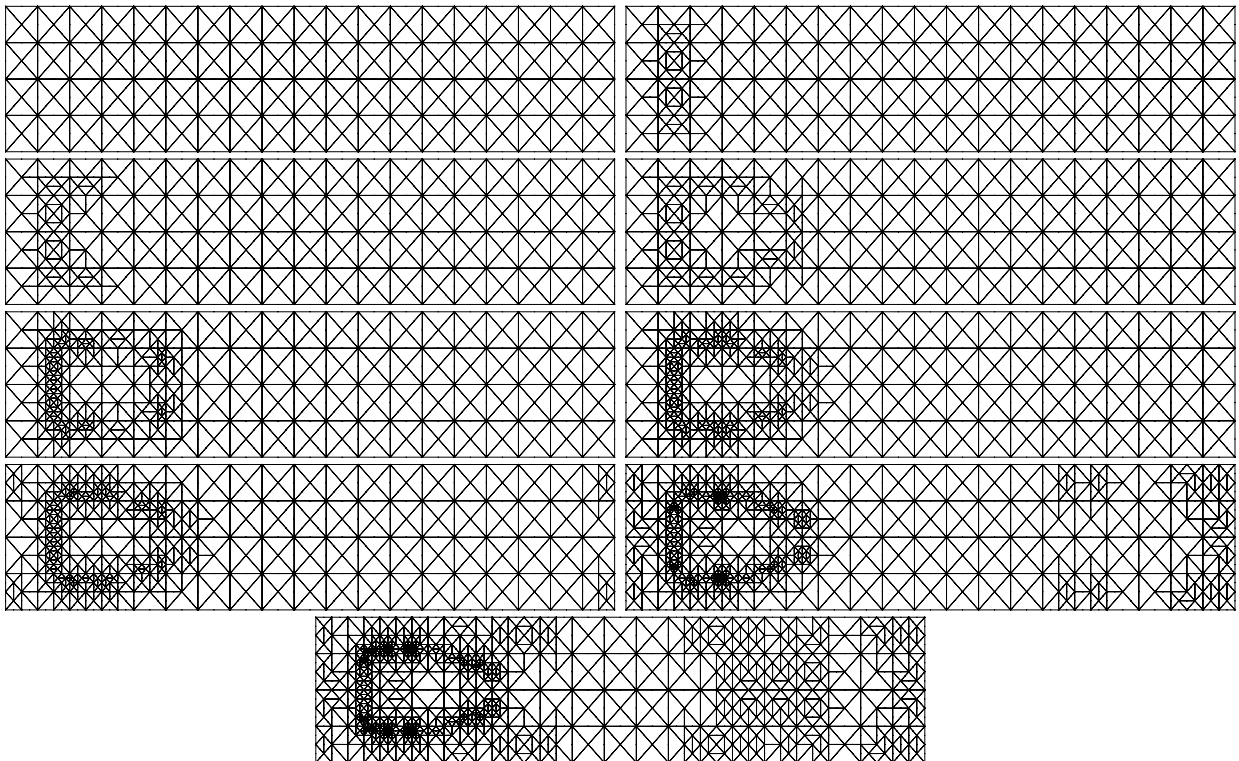


FIGURE 23. The sequence of meshes for the bearing problem.

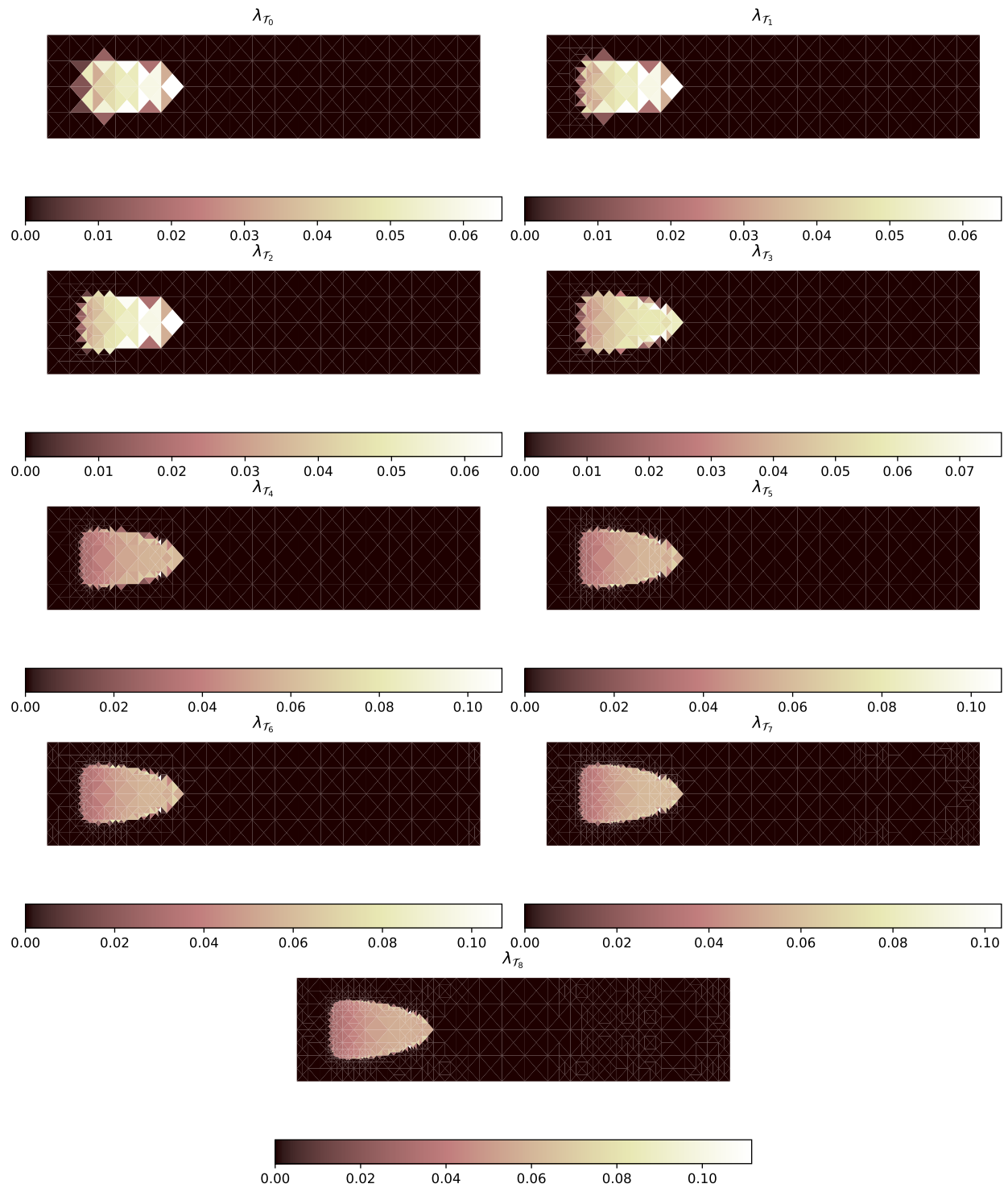


FIGURE 24. The sequence of Lagrange multipliers for the bearing problem.

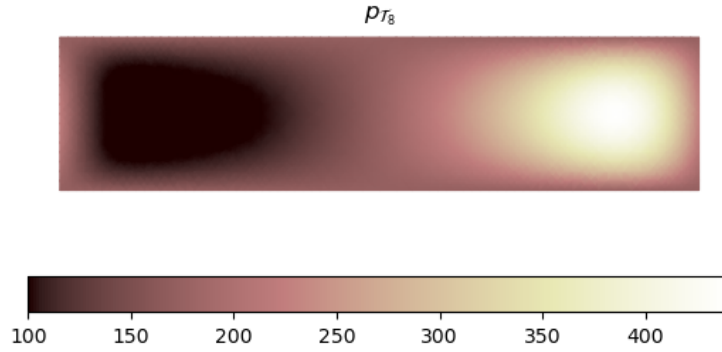


FIGURE 25. The pressure for the bearing problem.

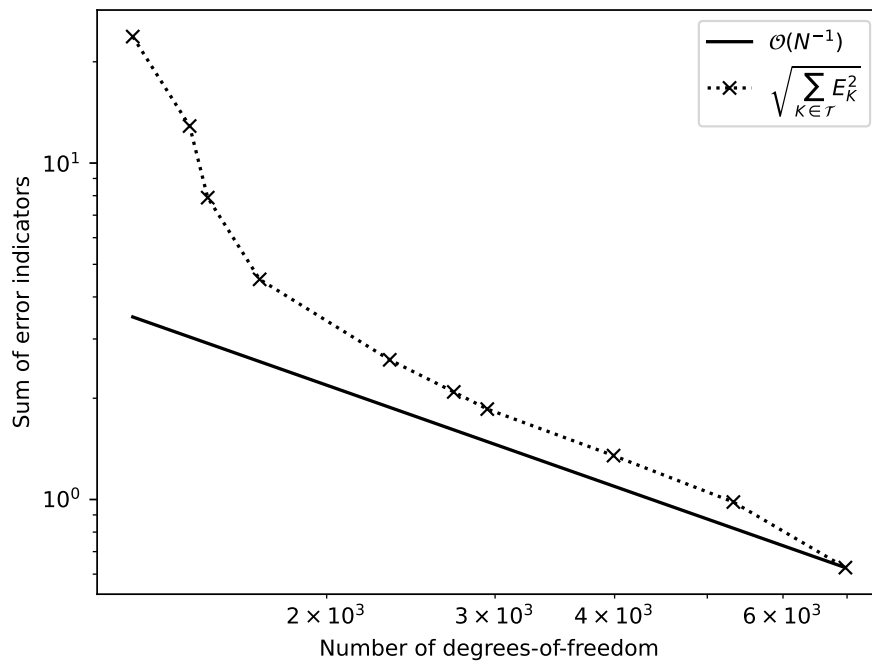


FIGURE 26. The total error for the bearing problem.

For the obstacle problems presented in this chapter, the finite element error analysis is by now well understood and adaptive methods can be used. Presently, practical problems are most conveniently implemented using programmable solvers that have a built-in support for adaptive mesh refinement with quadratic or higher order geometry description. The examples in this chapter were computed using scikit-fem [26] which is a library of assembly routines for implementing finite element solvers in Python. The mesh generation was done using a variant of distmesh [32]. Other open source packages suitable for implementing the methods presented in this chapter include FreeFem++ [40], NGSolve [41] and FEniCSx [42].

REFERENCES

- [1] Tom Gustafsson, Rolf Stenberg, and Juha Videman. Mixed and stabilized finite element methods for the obstacle problem. *SIAM Journal on Numerical Analysis*, 55(6):2718–2744, 2017.
- [2] Franz Chouly, Tom Gustafsson, and Patrick Hild. A Nitsche method for the elastoplastic torsion problem. *ESAIM: Mathematical Modelling and Numerical Analysis*, 57(3):1731–1746, 2023.

- [3] Tom Gustafsson, Kumbakonam R Rajagopal, Rolf Stenberg, and Juha Videman. An adaptive finite element method for the inequality-constrained Reynolds equation. *Computer Methods in Applied Mechanics and Engineering*, 336:156–170, 2018.
- [4] Michel Chipot. *Variational Inequalities and Flow in Porous Media*, volume 52 of *Applied Mathematical Sciences*. Springer Science & Business Media, 1984.
- [5] Lawrence C Evans. *An Introduction to Stochastic Differential Equations*. American Mathematical Society, 2012.
- [6] Tom Gustafsson, Rolf Stenberg, and Juha Videman. A stabilised finite element method for the plate obstacle problem. *BIT Numerical Mathematics*, 59(1):97–124, 2019.
- [7] Tom Gustafsson, Rolf Stenberg, and Juha Videman. On Nitsche’s method for elastic contact problems. *SIAM Journal on Scientific Computing*, 42(2):B425–B446, 2020.
- [8] Tom Gustafsson and Juha Videman. Stabilized finite elements for Tresca friction problem. *ESAIM: Mathematical Modelling and Numerical Analysis*, 56(4):1307–1326, 2022.
- [9] Tom Gustafsson and Philip L Lederer. Mixed finite elements for Bingham flow in a pipe. *Numerische Mathematik*, 152(4):819–840, 2022.
- [10] Franz Chouly, Patrick Hild, and Yves Renard. *Finite Element Approximation of Contact and Friction in Elasticity*, volume 48 of *Advances in Mechanics and Mathematics*. Springer Nature, 2023.
- [11] Jaroslav Haslinger, Ivan Hlaváček, and Jindřich Nečas. Numerical methods for unilateral problems in solid mechanics. *Handbook of numerical analysis*, 4:313–485, 1996.
- [12] Andreas Veese. Efficient and reliable a posteriori error estimators for elliptic obstacle problems. *SIAM Journal on Numerical Analysis*, 39(1):146–167, 2001.
- [13] Dietrich Braess. A posteriori error estimators for obstacle problems—another look. *Numerische Mathematik*, 101:415–421, 2005.
- [14] Alexander Weiss and Barbara I Wohlmuth. A posteriori error estimator for obstacle problems. *SIAM Journal on Scientific Computing*, 32(5):2627–2658, 2010.
- [15] Andreas Schröder. Mixed finite element methods of higher-order for model contact problems. *SIAM Journal on Numerical Analysis*, 49(6):2323–2339, 2011.
- [16] Tom Gustafsson, Rolf Stenberg, and Juha Videman. On finite element formulations for the obstacle problem—mixed and stabilised methods. *Computational Methods in Applied Mathematics*, 17(3):413–429, 2017.
- [17] Erik Burman, Peter Hansbo, Mats G Larson, and Rolf Stenberg. Galerkin least squares finite element method for the obstacle problem. *Computer Methods in Applied Mechanics and Engineering*, 313:362–374, 2017.
- [18] Robert A Adams and John JF Fournier. *Sobolev spaces*. Elsevier, 2003.
- [19] Kang Feng and Zhong-Ci Shi. *Mathematical theory of elastic structures*. Springer-Verlag Berlin Heidelberg, 1996.
- [20] Haïm Brézis and Moïse Sibony. Équivalence de deux inéquations variationnelles et applications. *Archive for rational mechanics and analysis*, 41:254–265, 1971.
- [21] Osborne Reynolds. IV. On the theory of lubrication and its application to Mr. Beauchamp Tower’s experiments, including an experimental determination of the viscosity of olive oil. *Philosophical Transactions of the Royal Society of London*, (177):157–234, 1886.
- [22] Andras Z Szeri. *Fluid Film Lubrication*. Cambridge University Press, 2010.
- [23] Tom Gustafsson, KR Rajagopal, Rolf Stenberg, and Juha Videman. Nonlinear Reynolds equation for hydrodynamic lubrication. *Applied Mathematical Modelling*, 39(17):5299–5309, 2015.
- [24] Minel J. Braun and William M. Hannon. Cavitation formation and modeling. In Q. Jane Wang and Yip-Wah Chung, editors, *Encyclopedia of Tribology*, pages 318–334. Springer Science & Business Media, 2013.
- [25] Michael Hintermüller, Kazufumi Ito, and Karl Kunisch. The primal-dual active set strategy as a semismooth Newton method. *SIAM Journal on Optimization*, 13(3):865–888, 2002.
- [26] Tom Gustafsson and G. D. McBain. scikit-fem: A Python package for finite element assembly. *Journal of Open Source Software*, 5(52):2369, 2020.
- [27] Rüdiger Verfürth. *A posteriori error estimation techniques for finite element methods*. Oxford University Press, 2013.
- [28] Dietrich Braess, Carsten Carstensen, and Ronald HW Hoppe. Convergence analysis of a conforming adaptive finite element method for an obstacle problem. *Numerische Mathematik*, 107:455–471, 2007.
- [29] Charles R Harris, K Jarrod Millman, Stéfan J Van Der Walt, Ralf Gommers, Pauli Virtanen, David Cournapeau, Eric Wieser, Julian Taylor, Sebastian Berg, Nathaniel J Smith, et al. Array programming with NumPy. *Nature*, 585(7825):357–362, 2020.
- [30] Pauli Virtanen, Ralf Gommers, Travis E Oliphant, Matt Haberland, Tyler Reddy, David Cournapeau, Evgeni Burovski, Pearu Peterson, Warren Weckesser, Jonathan Bright, et al. SciPy 1.0: fundamental algorithms for scientific computing in Python. *Nature methods*, 17(3):261–272, 2020.
- [31] John D Hunter. Matplotlib: A 2D graphics environment. *Computing in science & engineering*, 9(03):90–95, 2007.
- [32] Per-Olof Persson and Gilbert Strang. A simple mesh generator in MATLAB. *SIAM Review*, 46(2):329–345, 2004.
- [33] Elif Boru. Torsional strengthening of steel I beams with different GFRP configurations. *Structures*, 56, 2023.
- [34] I. Etsion and L. P. Ludwig. Observation of Pressure Variation in the Cavitation Region of Submerged Journal Bearings. *Journal of Lubrication Technology*, 104(2):157–163, 04 1982.
- [35] MJ Braun and RC Hendricks. An experimental investigation of the vaporous/gaseous cavity characteristics of an eccentric journal bearing. *ASLE transactions*, 27(1):1–14, 1984.

- [36] Huihui Feng, Shuyun Jiang, and Aimin Ji. Investigations of the static and dynamic characteristics of water-lubricated hydrodynamic journal bearing considering turbulent, thermohydrodynamic and misaligned effects. *Tribology International*, 130:245–260, 2019.
- [37] Yves Renard. Generalized Newton’s methods for the approximation and resolution of frictional contact problems in elasticity. *Computer Methods in Applied Mechanics and Engineering*, 256:38–55, 2013.
- [38] Franz Chouly. An adaptation of Nitsche’s method to the Tresca friction problem. *Journal of Mathematical Analysis and Applications*, 411(1):329–339, 2014.
- [39] Rodolfo Araya and Franz Chouly. Residual a posteriori error estimation for frictional contact with Nitsche method. *Journal of Scientific Computing*, 96(3):87, 2023.
- [40] Frédéric Hecht. New development in FreeFem++. *Journal of Numerical Mathematics*, 20(3-4):251–266, 2012.
- [41] Peter Gangl, Kevin Sturm, Michael Neunteufel, and Joachim Schöberl. Fully and semi-automated shape differentiation in NGSolve. *Structural and Multidisciplinary Optimization*, 63:1579–1607, 2021.
- [42] Igor A. Baratta, Joseph P. Dean, Jorgen S. Dokken, Michal Habera, Jack S. Hale, Chris N. Richardson, Marie E. Rognes, Matthew W. Scroggs, Nathan Sime, and Garth N. Wells. DOLFINx: the next generation FEniCS problem solving environment. preprint, 2023.